Influence of Agricultural Managed Aquifer Recharge and Stratigraphic Heterogeneities on Nitrate Reduction in the Deep Subsurface

Hannah Waterhouse[1,2*], Bhavna Arora[3], Nicolas F. Spycher[3], Peter S. Nico[3], Craig Ulrich[3], Helen E. Dahlke[1], and William R. Horwath[1]

Key Points:

- AgMAR variably impacts the timing and quantity of nitrate loading to groundwater as a function of vadose zone stratigraphy
- Under AgMAR, finer textured sediments are important reducing zones acting as permanent sinks of nitrate via denitrification
- Applying large amounts of water all-at-once under AgMAR rather than in small incremental amounts increases denitrification

[1] Land, Air and Water Resources, University of California at Davis; [2] Now at Environmental Science, Policy and Management, University of California at Berkeley; and [3] Lawrence Berkeley National Laboratory

* *Corresponding Author: Hannah Waterhouse*, Environmental Science, Policy, and Management, UC Berkeley, Mulford Hall, 130 Hilgard Way, Berkeley, California 94720; Tel: 310-666-3902; ORCID: 0000-0002-8387-4453 Email: *hwaterhouse@berkeley.edu*

Abstract

Agricultural managed aquifer recharge (AgMAR) is a proposed management strategy whereby surface water flows are used to intentionally flood croplands with the purpose of recharging underlying aquifers. However, legacy nitrate (NO_3^-) contamination in agriculturally-intensive regions poses a threat to groundwater resources under AgMAR. To address these concerns, we use a reactive transport modeling framework to better understand the effects of AgMAR management strategies (i.e., by varying the frequency, duration between flooding events, and amount of water) on N leaching to groundwater under different stratigraphic configurations and antecedent moisture conditions. In particular, we examine the potential of denitrification and nitrogen retention in deep vadose zone sediments using variable AgMAR application rates on two-dimensional representations of differently textured soils, soils with discontinuous bands/channels, and soils with preferential flow paths characteristic of typical agricultural field sites. Our results indicate that finer textured sediments, such as silt loams, alone or embedded within high flow regions, are important reducing zones providing conditions needed for denitrification. Simulation results further suggest that applying recharge water all-at-once, rather than in increments, increases denitrification within the vadose zone, but transports higher concentrations of NO_3^- deeper into the profile. This transport into deeper depths can be aggravated by wetter antecedent soil moisture conditions. We conclude that ideal AgMAR management strategies can be designed to enhance denitrification in the subsurface and reduce N leaching to groundwater, while specifically accounting for lithologic heterogeneity, antecedent soil moisture conditions, and depth to the water table.

Keywords: Nitrate, Agricultural Management, Groundwater Banking, Spatial variability, Managed Aquifer Recharge

1. Introduction

Nitrate (NO_3^-) contamination of freshwater resources from agricultural regions is an environmental and human health concern worldwide (Rodell et al. 2018). In agriculturally intensive regions, it is imperative to understand how management practices can enhance or mitigate the effect of nitrogen loading to freshwater systems. In California, managed aquifer recharge on agricultural lands is a proposed management strategy to counterbalance unsustainable groundwater pumping practices. Agricultural managed aquifer recharge (AgMAR) is an approach in which legally and hydrologically available surface water flows are captured and used to intentionally flood croplands with the purpose of recharging underlying aquifers (Kocis and Dahlke, 2017). AgMAR represents a shift away from the normal hydrologic regime wherein high efficiency irrigation application occurs mainly during the growing season. In contrast, AgMAR involves applying large amounts of water over a short period during the winter months. This change in winter application rates has the potential to affect the redox status of the unsaturated (vadose) zone of agricultural regions with implications for nitrogen (N) fate and transport to freshwater resources.

Most modeling studies targeting agricultural N contamination of groundwater are limited to the root zone; these studies assume that once NO_3^- has leached below the root zone, it behaves as a conservative tracer until it reaches the underlying groundwater (Harter et al. 2008, Botros et al. 2012, van der Laan et al. 2013, Baram et al. 2016, Ascott et al. 2016 & 2017) or, these studies

employ first order decay coefficients to simplify N cycling reactions (Hanson et al. 2006, Phogat et al. 2014, Salehi et al. 2017). However, recent laboratory and field-based investigations in agricultural systems with deep unsaturated zones have shown the potential for N cycling, in particular denitrification, well below the root zone (Xiang et al. 2008, Jahangir et al. 2012, Peterson et al. 2013, Pratt et al. 1972). Moreover, in agricultural settings, especially in alluvial basins such as in California with a history of agriculture, large amounts of legacy NO_3^- has built up over years from fertilizer use inefficiencies and exists within the deep subsurface (Van Meter et al. 2016, Waterhouse et al. 2020). It is not yet clear how this legacy nitrogen may respond to changing hydrologic regimes and variations in AgMAR practices, and more importantly, if flooding agricultural sites is enhancing nitrate transport to the groundwater or attenuating it by supporting *in situ* denitrification.

Several studies have documented that denitrification rates in the deep subsurface vary as a function of NO_3^-, carbon, and oxygen concentrations as well as other environmental factors (e.g., pH, temperature, texture, iron) (Arora et al., 2013; Dwivedi et al., 2018; Yabusaki et al., 2017). While total soil organic carbon typically declines with depth (Syswerda et al. 2011), dissolved organic carbon (DOC) can be readily transported by water lost from the root zone to deeper layers (Bundt et al. 2001, Jardine et al. 2006) and can therefore be available to act as an electron donor for denitrification (Peterson et al. 2013, Cressey et al. 2018). Oxygen concentration in the vadose zone is maintained by advective and diffusive transport, while oxygen consumption occurs via microbial metabolic demand and/or abiotic chemical reactions (Akhavan et al. 2013, Dutta et al. 2015). The effects of drying and wetting cycles on oxygen (O_2) concentrations in the deep subsurface are not well documented, however, there is some evidence that O_2 consumption proceeds rapidly as saturation increases and rebounds quickly during dry periods (Dutta et al. 2015). These variations in oxygen concentration can influence N cycling and, thus, transport to groundwater. Therefore, a gap currently exists in quantifying N attenuation and transport from agriculturally intensive regions with a “deep” vadose zone while accounting for the many competing N cycle reactions and transformations, as impacted by different hydrological regimes imposed under AgMAR.

The application of AgMAR itself can vary in terms of the hydraulic loading and rates used, as well as the duration between flood water applications. These can in turn affect water retention times, O_2 availability, consumption of electron donors (carbon) and consequently , denitrification rates (Akhavan et al. 2013). For example, denitrification rates were found to increase with increased hydraulic loading and with shorter times between flood applications within the vadose zone of a rapid infiltration basin system used for disposing of treated wastewater (Akhavan et al. 2013). In shallow, sandy soils, high flow rates - above an infiltration threshold - were negatively correlated with denitrification rates, suggesting that an optimum infiltration rate exists for a given sediment stratigraphy to maximize NO_3^- reduction (Schmidt et al. 2011). Given the immense stratigraphic heterogeneity in alluvial basins, such as in California’s Central Valley, a range of optimum infiltration rates may exist with implications for managing AgMAR differently based on the geologic setting of the intended site. Therefore, the objectives of this study are to: a) understand the effects of varying stratigraphy and hydrologic regimes on denitrification rates, and b) identify AgMAR management scenarios that increase denitrification rates, such that the potential for N leaching to groundwater is decreased.

Herein, we focus on an agricultural field site in Modesto, California located within the Central Valley of California, which is responsible for California’s $46 billion-dollar agricultural

economy (CDFA, 2017). The field site typifies the deep vadose zones prevalent in this region, which are characterized by heterogenous layered alluvial sediments intercalated with discontinuous buried clay and carbon rich paleosols (Weissman et al. 2002a, 2002b, Bennet et al. 2006, Chaopricha and Marín-Spiotta, 2014, Marín-Spiotta et al. 2014). These banded features, especially the paleosols, as well as areas of preferential flow, are typically associated with enhanced biogeochemical activity, higher carbon content and availability of metabolic substrates such as nitrogen (Brockman et al. 1992, Bundt et al. 2001). These regions respond to and change depending on environmental conditions such as water content and oxygen concentration *in situ* that are influenced by the hydrologic regime at the surface and may be important for NO_3^- attenuation and reduction prior to reaching the water table. Therefore, this study considers varying hydrologic regimes and stratigraphic variations (including preferential flow paths and discontinuous bands/channels) that are prevalent in the region. More specifically, at the Modesto field site (which is described in more detail below), large amounts of legacy N already reside in the vadose zone, while N fertilizer application and irrigation occurs throughout the spring and summer months. AgMAR, if implemented, occurs during the winter months as water becomes available. Therefore, we focus here on quantifying the effects of AgMAR on N cycling in the deep vadose zone and implications for NO_3^- contamination of groundwater at this characteristic agricultural field site. We also investigate the specific AgMAR application rates that would increase the effectiveness of *in situ* denitrification under different stratigraphic configurations through the development and testing of a reactive transport model. We believe such an analysis provides important insights for the successful application of AgMAR strategies aimed at improving groundwater storage in a changing climate.

2. Modeling Strategy

Reactive transport models can be beneficial tools to elucidating N fate and transport in deep vadose zone environments. Herein, we develop a comprehensive reaction network incorporating the major processes impacting N transport and attenuation, such as aqueous complexation, mineral precipitation and dissolution, and microbially mediated redox reactions. While using the same reaction network, we implement several numerical scenarios to quantify the range of denitrification rates possible under different AgMAR implementation strategies and stratigraphic configurations (Figure 1 & Figure 2). For the latter, we used four different stratigraphic configurations with a low permeability layer on top including i) two homogeneous textural profiles, ii) a sand stratigraphy with a discontinuous silt band, iii) a silt stratigraphy with a discontinuous sand band, and iv) a complex stratigraphy more representative of the field conditions investigated by electrical resistance tomography (ERT). The top layer was specifically calibrated to match measured average field infiltration rates of 0.17 cm/hr. For each stratigraphy, we further varied the frequency and duration of water per application to investigate the impact of different AgMAR implementations that are similar to recent field trials conducted throughout the state (Bachand et al. 2014). In addition, we tested the effect of antecedent moisture conditions on N biogeochemistry within the more complex stratigraphy by setting the model with a wetter initial moisture profile. Overall, a set of 18 simulation experiments were used to isolate and understand the contribution of different AgMAR strategies to enhance or decrease denitrification rates in deep vadose zone environments with homogeneous and banded configurations. A detailed model setup and numerical implementation is provided in Section 4.

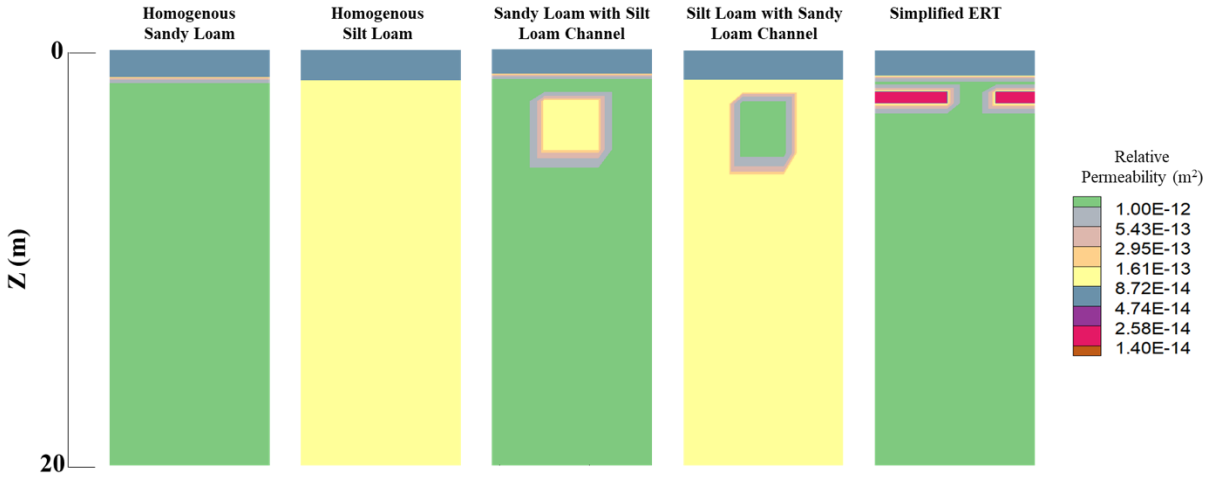

Figure 1: Five varying stratigraphic profiles based on structural features from ERT profiles.

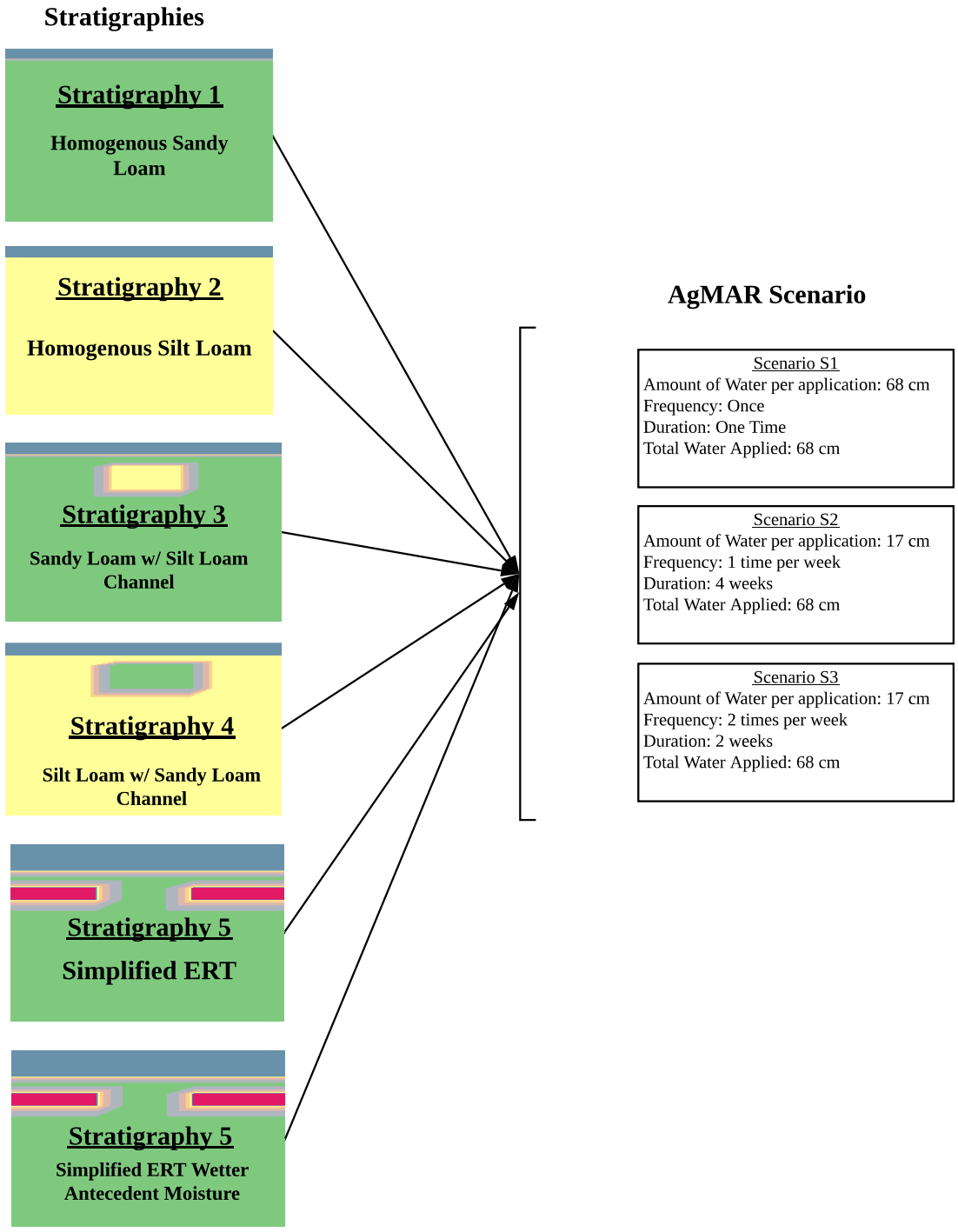

Figure 2: Conceptual diagram of modeling scenarios including the five stratigraphy scenarios overlain by each AgMAR management scenario (S1 to S3).

3. Field Site and Datasets

3.1. Study Site

The study site is an almond orchard located in California's Central Valley, southwest of Modesto, and north of the Tuolumne River (Figure 3). The surface soil is classified as a Dinuba fine sandy loam (coarse-loamy, mixed, active, thermic, Typic Haploxeralf). The site is characterized by a Mediterranean climate, with wet winters and hot, dry summers. Average annual temperature and total annual precipitation are 17.5° C and 335 mm, respectively. As suggested above, the vadose zone typifies the valley with contrasting layered sequences of granitic alluvial sedimentary deposits consisting of predominantly silt loams and sandy loams. We therefore use these textures to design our modeled stratigraphic configurations with and without banded layers. The groundwater table in the study area typically occurs around 15 m below ground surface. Soil properties including percent sand, silt, clay, total N, total C, and pH are shown in Table 1.

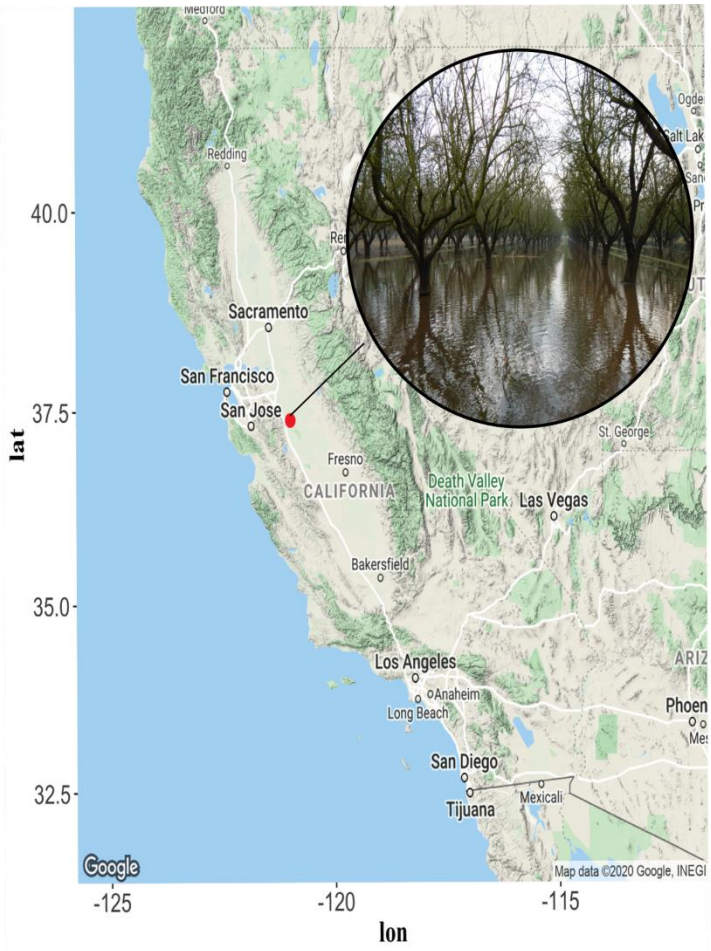

Figure 3: Map of study area in Modesto, CA with a picture of the actual field site during an AgMAR flooding event.

Table 1: Soil properties averaged by depth (per meter) with standard errors in parentheses (n=5/meter).

Depth (cm)	Sand (%)	Silt (%)	Clay (%)	Total N (%)	Total C (%)	NO_3^--N (ug/g)	pH
0-25	46.24 (7.68)	46.13 (7.49)	7.64 (0.72)	0.048 (0.01)	0.73 (0.11)	10.19 (4.18)	6.71 (0.15)
100-200	42.41 (6.49)	48.64 (5.53)	8.95 (2.64)	0.050 (0.03)	0.21 (0.04)	13.81 (4.63)	6.99 (0.10)
200-300	48.39 (9.57)	43.19 (8.16)	8.43 (2.57)	0.050 (0.03)	0.068 (0.02)	5.09 (1.38)	6.99 (0.09)
300-400	56.09 (9.93)	37.64 (8.36)	6.27 (1.71)	0.010 (0.01)	0.048 (0.02)	3.26 (1.07)	6.99 (0.10)
400-500	78.96 (8.13)	18.12 (7.42)	2.92 (0.78)	0.004 (0.001	0.056 (.03)	1.11 (0.34)	6.92 0.07)
500-600	55.60 (7.39)	33.34 (5.54)	11.06 (2.14)	0.006 (0.001	0.065 (0.02)	1.37 (0.31)	7.07 (0.07)
600-700	60.56 (8.05)	35.38 (7.47)	4.06 (1.21)	0.060 (0.05)	0.035 (0.02)	0.57 (0.13)	7.18 (0.07)
700-800	75.45 (4.93)	16.59 (3.63)	7.96 (1.44)	0.120 (0.07)	0.027 (0.01)	0.83 (0.17)	7.26 (0.09)
800-900	84.11 (4.27)	10.56 (3.63)	5.33 (1.35)	0.020 (0.01)	0.099 (0.02)	1.71 (0.37)	7.17 (0.11)

3.2. Characterization of the Deep Vadose Zone

To specifically characterize the textural layers and subsurface heterogeneity at our site, we used electrical resistivity tomography (ERT) (Ulrich et al. 2020, in preparation). ERT profiles were generated along a 150 m transect to 20 m depth prior to flooding to quantify subsurface heterogeneity while the subsurface was relatively dry (Figure 4). Further, to validate the texture profiles generated by the ERT data, a set of six cores were taken along the transect of the ERT line down to nine meters with a Geoprobe push-drill system (Geoprobe Systems, Salina, KS). The first meter of the core was sampled every 25 cm. Thereafter, cores were sampled based on stratigraphy as determined by changes in color or texture. The ERT profiles were used to develop the stratigraphic modeling scenarios and the coring guided the specification of the hydraulic parameters. Redoximorphic features (i.e., changes in concentration and depletion of Fe) were noted throughout the cores.

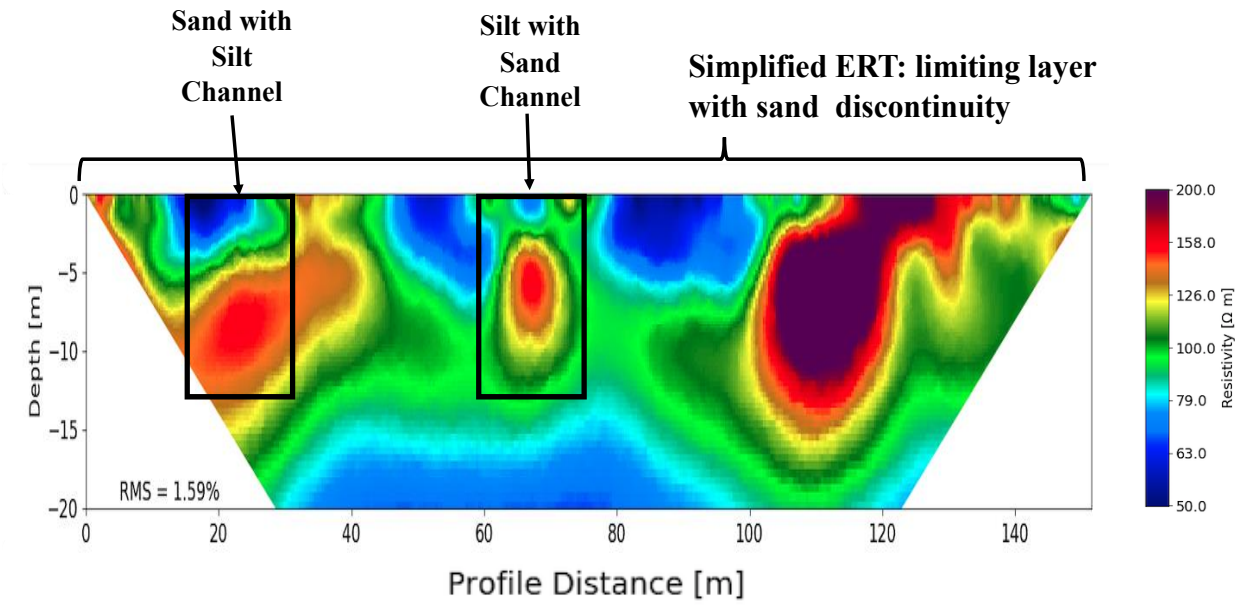

Figure 4: Electrical resistivity tomography image of a 2D transect at our field site. More conductive layers are in blue and more resistive layers are in red.

3.3. Soil and Vadose Zone Physical and Chemical Analysis

Texture was analyzed using a modified pipette method whereby 5 g of soil were placed in 50 mL centrifuge tubes with 40 mL of 0.5% sodium phosphate and shaken overnight (Soil Survey Laboratory Methods Manual, 2004). Samples were hand shaken immediately before a 2.5 mL aliquot was taken 11 seconds (sand fraction) and 1 hour and 51 minutes (clay fraction), respectively after shaking and placed in a pre-weighed tin. Tins were oven dried at 105°C overnight and reweighed the next day. Silt fractions were calculated by subtracting the sand and clay fraction from 1.

Nitrate (NO_3^-) and ammonium (NH_4^+) were analyzed by weighing 8-10 g of soil into a 50-mL centrifuge tube and extracted with 2M KCl. Samples were centrifuged and the supernatant was analyzed colorimetrically for soil NO_3^- and NH_4^+ using a UV mini 1240, Shimadzu spectrophotometer as per methods described in Doane and Horwath (2003). Gravimetric water content was determined after soil samples were dried over night at 105° C. Total nitrogen (N) and soil organic carbon (SOC) were measured via combustion on a Costech ECS 4010 CHNSO elemental analyzer using soil samples that were dried at 60° C and pulverized using a ball mill. Samples were checked for carbonates using a 1 mol L^{-1} hydrochloric acid (HCl) solution prior to combustion. A 1:1 water to soil ratio was placed in a falcon tube, shaken for an hour, allowed to settle, and the supernatant pH measured (Thomas, 1996).

Total reactive iron was measured by extracting 1 g of soil with 0.25 M hydroxylamine hydrochloride and 0.25 M HCl, shaking for 1 hour, and reacting with ferrozine (3-(2-pyridyl)-5,6-diphenyl-1,2,4-triazine-4',4"-disulfonate) and measured at 565 nm on a spectrophotometer (Lovley and Phillips 1987, Stookey 1970, Violler et al. 2000). Sulfur and manganese were determined on the supernatant of the same solution by the UC Davis ICPMS. Using a 1:4 ratio of soil to 0.5 M K_2SO_4, dissolved organic carbon (DOC) was extracted, shaken for 1 hour,

centrifuged for 10 min at 3000xg, and analyzed on a UV-persulfate total organic carbon analyzer (Phoenix 8000, Tekmar Dohrmann™, Cincinnati, OH).

3.4. Acetylene Inhibition Method for Measuring Denitrification Capacity for Model Development

Soil cores taken after the AgMAR event were used to carry out microcosm experiments under anaerobic conditions in a helium atmosphere at 22°C to determine denitrification capacity according to a modified method by Groffman et al. (1999) and detailed in Waterhouse et al. (2020, in prep). The N_2O and CO_2 measurements after the third and final day of the incubation were used to inform the reaction rate parameters for denitrification. In particular, we used the Q10 equation to adjust the reaction parameters. This is because the Q10 equation can account for the temperature sensitivity of the reaction by calculating the change in the rate of a reaction given a 10 °C change in temperature (Kirschbaum, 1995). Given that our field site temperatures were lower during the winter (mean of 18 °C) than the temperatures at which the denitrification capacity assays were incubated, we estimated the reaction rate using the following equation (Meyer et al. 2018):

$$R_2 = R_1 \, x \, Q_{10}^{(T_2 - T_1)/10} \quad [1]$$

where R_1 and R_2 are the reaction rates at two different temperatures, T_1 and T_2 (°C), respectively, and Q_{10} is the factor by which the reaction rate increases when the temperature is raised by ten degrees.

4. Description of the Modeling Framework

4.1. Statistical Analysis

Exploratory data analysis was performed on all physical and geochemical measurements collected on the soil cores to establish normality conditions (or lack thereof). Almost all variables were found to be non-normally distributed based on the Kolmogorov-Smirnov test. Therefore, we used only conservative, non-parametric statistics to analyze the complete dataset involving variables like pH, N_2O, NO_3^-, NH_4^+, DOC, Fe, Mn, S, total C, percent sand, silt, and clay, and depth. Variables were standardized using the median and mean absolute distance and a Spearman's rank correlation was conducted on the dataset. Correlation analysis was used to delineate the impact of spatial layering or textural heterogeneity on N concentrations, if any. Correlations between variables with p-values less than 0.05 were considered to be significant. To further understand how the data grouped, a cluster analysis was conducted using the partitioning around medoids method. Interestingly, data were found to group according to textural classes and depth, which provides a mechanism to formulate the modeling framework.

4.2. Simulation Model

We used the reactive transport code TOUGHREACT V3.32-OMP (Xu et al. 2017, Sonnenthal et al. 2014) to quantify the fate and transport of nitrogen in the deep vadose zone of our study site. For this study, the EOS3 module of TOUGHREACT was used to simulate coupled isothermal, multiphase (water and air) flow and multicomponent reactive transport in the vadose zone (Sonnenthal et al. 2014; Pruess et al. 1999).

4.2.1. Model Setup and Scenarios

Several scenarios were developed based on the soil textures identified in cores and the ERT profiles to provide insights into the effect of stratigraphic heterogeneity and AgMAR management strategies on NO_3^- cycling in the deep subsurface, as described in section 2 above. The five stratigraphies modeled in this study are shown in Figure 1. The claypan in the ERT scenario spans 187 cm to 234 cm based on field observations. For each lithologic profile, three AgMAR management strategies were imposed at the top boundary between 20 m and 150 m of each modeled profile (Figure 2). For each AgMAR management strategy, the same overall amount of water was applied, but the frequency, duration between flooding events, and amount of water applied in each flooding event varied (as shown in Figure 2): a total of 68 cm of water was applied either all at once (scenario S1), in increments of 17 cm once a week for four weeks (scenario S2), in increments of 17 cm twice a week for two weeks (scenario S3), and all three scenarios with an initially wetter moisture profile (Figure 2). Note, that for all scenarios, the same reactions were considered, the water table was maintained at 15 m, and temperature was fixed across depths at 18°C, the mean air temperature for January to February in Modesto.

For all scenarios, the modeling domain consists of a two-dimensional 20-meter deep vertical cross-section extending laterally 2,190 m and including a 190 m wide zone of interest located at its center, thus distant from lateral boundaries on each side by 1,000 m to avoid boundary effects. The zone of interest was discretized using a total of 532 grid blocks with a uniform grid spacing of 1 m along the horizontal axis, and a grid spacing of 0.02 m in the unsaturated zone increasing with depth to 1 m in the saturated zone. A maximum time step of 1 day was specified for all simulated scenarios, although the actual time step was limited by specifying a Courant Number of 0.5, typically resulting in much smaller time steps during early stages of flooding.

Before each flooding simulation, the model was run first to hydrologic steady state conditions including the effect of average (background) rainfall (33 cm $year^{-1}$). The water table was set at a depth of 15 m by specifying a constant pressure at the bottom model boundary (1.5×10^5 Pa at a depth of 20 m), and the model side boundaries (1000 m away from the zone of interest) were set to no-flow conditions.

Under these hydrologic conditions, the model was then run for a 100-yr time period including biogeochemical reactions and fixed atmospheric conditions of O_2 and CO_2 partial pressures at the top boundary, a period after which essentially steady biogeochemical conditions were achieved, including the development of progressively reducing conditions with depth representative of field conditions. For these simulations, the concentrations of dissolved species in background precipitation and in groundwater at the bottom model boundary were fixed, with compositions described in Table 2 to yield similar vertically distributed NO_3^- concentrations as were measured in the soil cores.

Flooding scenarios were then started from the initially steady flow and biogeochemical conditions developed as described above. For these simulations, a free surface boundary was implemented for scenario S1 where 68 cm of water was applied all at once. In contrast, a specified flux boundary condition was imposed for the scenarios S2-S3, where floodwater applications were broken up over a week. The flood water composition is discussed in Section 4.4.

Table 2: Aqueous concentrations of primary species applied as fixed concentrations at the top of the model boundary and in the flood water. Concentrations are in mol L^{-1}, unless otherwise specified.

	Initial Water	Flood Water
pH[(a)]	7.5	8[b]
$O_{2\ (aq)}$	2.0947×10^{-4}	2.0947×10^{-4} [c]
$SiO_{2\ (aq)}$	6.8266×10^{-4}	6.8266×10^{-6}
Na^{+}	1.8276×10^{-3}	1.8276×10^{-5}
K^{+}	7.4203×10^{-5}	7.4203×10^{-7}
Ca^{2+}	9.7350×10^{-4} [d]	9.7350×10^{-6}
Mg^{2+}	3.4986×10^{-4}	3.4986×10^{-6}
HCO_3^{-}	4.0580×10^{-3} [d]	1.6545×10^{-5} [e]
SO_4^{2-}	1.2497×10^{-4}	1.2497×10^{-6}
Cl^{-}	6.7723×10^{-4}	6.7723×10^{-4}
HS^{-}	1.0000×10^{-20}	1.0000×10^{-20}
NO_3^{-}	7.1378×10^{-4}	7.1378×10^{-6}
NO_2^{-}	9.3504×10^{-7}	9.3504×10^{-9}
N_2	1.0000×10^{-20}	1.0000×10^{-20}
$NH_{3\ (aq)}$	1.0000×10^{-8}	1.0000×10^{-9}
Al^{3+}	6.6965×10^{-10} [f]	1.0000×10^{-20}
Fe^{3+}	1.1582×10^{-19} [g]	1.0000×10^{-20}
Fe^{2+}	8.3000×10^{-20}	8.3000×10^{-20}
Ba^{2+}	4.1524×10^{-7}	1.0000×10^{-20}
Sr^{2+}	5.1722×10^{-6}	1.0000×10^{-20}
Acetate	1.1895×10^{-5} [h]	1.1895×10^{-7} [h]

[(a)] pH units
[(b)] adjusted for charge balance
[(c)] Fixed by P_{O2} (g) of $10^{-0.7}$ bar
[(d)] Fixed by equilibrium with calcite
[(e)] Fixed by P_{CO2} (g) of $10^{-3.4}$ bar
[(f)] Fixed by equilibrium with k-feldspar

[g] Fixed by equilibrium with ferrihydrite
[h] Fixed by equilibrium with cellulose

4.3. Hydrological and Transport Properties

The Rosetta pedotransfer function model (Schaap et al. 2001) was used to estimate van Genuchten-Mualem parameters for the dominant textural classes identified through cluster analyses (Section 5.1). The hydraulic properties of the top layer were adjusted to match the average infiltration rate of the field experiments of 0.17 cm/hr. Table 3 shows the van Genuchten-Mualem parameters used in this study. Relative permeability values were calculated from the saturated hydraulic conductivity.

Table 3: Hydraulic parameters used in this study. $K_{s,z}$ is the saturated hydraulic conductivity in the vertical direction, θ_r and θ_s are the residual and saturated volumetric water content, α is related to the inverse of the air entry pressure value, and *n* is soil water retention curve shape parameter.

Soil Type	Permeability, k (m^2)	$K_{s,z}$ (cm/hr)	van Genuchten-Mualem Parameters			
			n (-)	**α** (cm^{-1})	θ_r (-)	θ_s (-)
Top Layer - Modified Loam	4.8×10^{-14}	0.17	1.31	0.019	0.095	0.43
Claypan	1.4×10^{-14}	0.05	1.09	0.008	0.068	0.48
Silt Loam	1.3×10^{-13}	0.45	1.41	0.02	0.067	0.46
Sandy Loam	1.3×10^{-12}	4.4	1.89	0.075	0.065	0.41

4.4. Geochemical System

The key geochemical processes included in this study are aqueous speciation, ion exchange, mineral precipitation/dissolution reactions, and microbially mediated redox reactions. The primary species in the modeled reaction network include H^+, H_2O, $SiO_{2\,(aq)}$, Na^+, K^+, Ca^{+2}, Mg^{+2}, HCO_3^-, SO_4^-, Cl^-, $O_{2\,(aq)}$, HS^-, NO_3^-, NO_2^-, $N_{2\,(aq)}$, $NH_{3\,(aq)}$, Al^{+3}, Fe^{+3}, Fe^{+2}, Ba^{+2}, Sr^{+2}, and acetate. The aqueous complexation reactions and their equilibrium constants are listed in Table A1 in the Appendix.

The mineralogy of the agricultural field site (types and amounts of minerals constituting each soil type) was assigned on the basis of previous studies at nearby field locations with similar geology (Harden 1987, Neal et al. 1987, White et al. 1996). Based on these studies, quartz, k-feldspar, albite, montmorillonite, calcite, illite, ferrihydrite, and gibbsite were taken as the main soil constituents. All of these minerals are considered to react under kinetic constraints. The thermodynamic and kinetic constraints for mineral precipitation/dissolution reactions are listed in Tables A2 and A3 in the Appendix. Note that the amount of ferrihydrite in soil was

calibrated according to the ferrozine extractions described above, and amounts of other minerals estimated from the previously cited studies (Table A4).

The groundwater composition was taken from analyses reported by Landon and Belitz (2006) for a groundwater well (MOD-01) located near our study site. For simplicity, the background recharge from rainfall was assumed to have the same composition as groundwater except that it was re-equilibrated under atmospheric O_2 and CO_2 conditions prior to infiltration. In addition, the concentrations of N species in the background recharge were set to values determined from our own analyses of N at the top of soil cores. The composition of the flood water was set to that of the background precipitation diluted by a factor of 100 for most constituents except for Cl^{-1}. Ratios of NO_3^- to Cl^{-1} were used to trace the difference between dilution and denitrification effects on NO_3^-.

Denitrification and N_2O production were simulated as aqueous kinetic reactions coupled to the fate of pH, CO_2, Fe, S, NO_3^-, and NH_4^+ based on the Spearman correlation analyses discussed above ($p<0.05$). Apart from pH and nitrate species, Fe and S have been linked to denitrification through chemolithoautotrophic pathways (Arora et al. 2016, Carlson et al. 2012) in addition to heterotrophic denitrification (Butterbach et al. 2013), and are therefore included in our reaction network. Heterotrophic denitrification of NO_3^- to N_2 was represented via a two-step reduction process of NO_3^- to nitrite (NO_2^-) and NO_2^- to dinitrogen (N_2). Additionally, chemolithoautotrophic reduction of NO_3^- to N_2 with Fe (II) and bisulfide (HS^-) as electron donors were implemented. Further, dissolved organic carbon (DOC) was observed throughout the nine-meter profile at our field site, and CO_2 and N_2O profiles showed strong correlation ($p<0.05$). Therefore, DOC degradation was simulated using Monod kinetics, although individual DOC components were not simulated consistent with other modeling studies (Hunter et al. 1998, Arora et al. 2015). In particular, we considered a single solid phase of cellulose in equilibrium with acetate as the source of DOC. Parameters for cellulose dissolution were calibrated using the total organic carbon concentrations obtained for each cluster. Biodegradation of acetate was coupled to multiple terminal electron acceptors, including NO_3^-, Fe (III) and SO_4^{2-} which follow the hierarchical sequence of reduction potential of each constituent implemented by using inhibition terms that impede lower energy-yielding reactions when the higher energy yielding electron acceptors are present. These microbially mediated reactions and their kinetic rate parameters are shown in Table 5.

Rates for denitrification were calibrated using the results from the acetylene inhibition assays as described above. Enzymes involved in denitrification include nitrate reductase, nitrite reductase and nitrous oxide reductase. To remain conservative in our estimates, we chose values typical for oxygen inhibition of nitrous oxide reductase (0.01 mg $O_{2\,(aq)}$ L^{-1}), the most sensitive to oxygen of the enzymes (Bonin et al. 1989).

Table 4: Microbially mediated redox reactions, their thermodynamic and kinetic parameters considered in the reactive transport model.

Reaction	**Log K (25 °C)[(a)]**	**K_{max}**	**K_s**	**$K_{inibitor}$**
		(mol L^{-1} s^{-1})	**(mol L^{-1})**	**(mol L^{-1})**

$CH_3COO^- + 2O_2 \rightarrow 2HCO_3^- + H^+$	146.76	1.0×10^{-11} [b]	O_2: 2.41×10^{-5} [d]	
$CH_3COO^- + 4NO_3^- \rightarrow 2HCO_3^- + 4NO_2^- + H^+$	89.04	2.78×10^{-10} [c]	NO_3^-: 1.13×10^{-4} [d]	O_2: 3.22×10^{-7} [e]
$CH_3COO^- + 2.667NO_2^- + 1.667H^+ \rightarrow 2HCO_3^- + 1.33N_2 + 1.33H_2O$	200.52	3.47×10^{-8} [c]	NO_2^-: 1.13×10^{-4} [d]	O_2: 3.22×10^{-7} [e]
$NH_3(aq) + 2O_2 \rightarrow NO_3^- + H_2O + H^+$	62.23	5.27×10^{-2} [b]	NH_3: 1.48×10^{-5} [f] O_2: 2.41×10^{-5} [d]	
$CH_3COO^- + 8Fe^{+3} + 4H_2O \rightarrow 8Fe^{+2} + 2HCO_3^- + 9H^+$	79.00	1.0×10^{-14} [b]		O_2: 3.22×10^{-7} [e] NO_3^-: 1.0×10^{-7} [g]
$Fe^{+2} + 0.2NO_3^- + 1.2H^+ \rightarrow Fe^{+3} + 0.1N_2 + 0.6H_2O$	-7.32	7.0×10^{-10} [h]	Fe^{+2}: 1.0×10^{-5} [i] NO_3^-: 1.13×10^{-4} [d]	O2: 3.22 x 10-7 [e] NO3-: 1.0 x 10^{-7} [g]
$CH_3COO^- + SO_4^{-2} \rightarrow 2HCO_3^- + HS^-$	8.40	3.0×10^{-12} [b]	SO_4^{-2}: 1.0×10^{-3} [i]	O_2: 3.22 x 10-7 [e] NO_3^-: 1.0 x 10^{-7} [g] Fe^{+3}: 1.0 x 10^{-12} [b]
$HS^- + 1.6NO_3^- + 0.6H^+ \rightarrow SO_4^{-2} + 0.8N_2 + 0.8H_2O$	11.52	7.0×10^{-10} [j]	HS^-: 1.0×10^{-5} [k] NO_3^-: 1.13×10^{-4} [d]	O_2: 3.22×10^{-7} [e]

[a]Calculated from log*K* values for half redox reactions reported by (Morel and Hering 1993); [b]Adapted from Arora et al. 2016; [c]Calibrated using denitrification capacity assays; [d]Taken from Maggi et al. 2008; [e]Taken from Bonin et al. 1989; [f]Taken from Wu et al. 2011; [g] Taken from Doussan et al. 1997; [h]Adapted from Palmer et al. 2010; [i]Taken from Mayer et al. 2002; [j] Kept to yield maximum reaction rate similar to that of NO_3^- reduction by Fe^{+2}; [k]Taken from Handley et al. 2013

5. Results

5.1. Cluster Analysis

Cluster analysis was used to detect natural groupings in the soil data based on physio-chemical characteristics, textural classes and the total dataset. Cluster analysis revealed three clusters representing distinct depth associated textural classes with varying levels of substrates and biogeochemical activity. Table 6 shows the median and range for N_2O, CO_2, NO_3^- -N, Fe, S and total organic C for each of the clusters. The first cluster is dominated by sandy loams within the top meter with highest median values of total N_2O, total CO_2, NO_3^- -N, Fe, and total organic C concentrations, indicative of greatest microbial activity and denitrification potential. The second cluster is dominated by silt loams below one meter and had average values of total N_2O, total CO_2, NO_3^- -N, Fe, and total organic C concentrations when compared to the other groups. The third group is dominated by sands and sandy loams below 1 meter and had the lowest median values of total N_2O, total CO_2, NO_3^- -N, Fe, and total organic C concentrations amongst all groups. The clusters were thus automatically grouped by decreasing levels of denitrification and microbial activity. While most concentrations followed a decreasing concentration trend from cluster 1 to 3, the highest median values of S were associated with cluster 2.

Table 5: Results of cluster analysis on soil core and acetylene inhibition incubation data. Medians are shown with minimum and maximum values in parentheses.

	Soil Classification	Total N_2O	Total CO_2	TOC	NO_3^-	Fe	S
		ug g^{-1}	ug g^{-1}	%	ug g^{-1}	ug g^{-1}	ug g^{-1}
1	Sandy Loam top meter	1.62 (1.46-1.72)	175.30 (74.70-587.35)	0.18 (0.01 - 0.29)	1.20 (1.19 - 2.64)	14.77 (10.94 - 20.66)	0.44 (0.33 - 0.47)
2	Silt Loam below one meter	0.53 (0.40 - 0.80)	35.70 (15.10 - 61.97)	0.07 (0.03 - 0.16)	1.01 (0.80 - 1.84)	12.02 (8.64 - 14.96)	0.69 (0.41 - 1.20)
3	Sand and Sandy Loam below one meter	0.05 (0.01 - 0.015)	10.70 (0.0 - 59.40)	0.06 (0.03 - 0.10)	0.25 (0.0 - 0.70)	10.43 (7.27-16.34)	0.44 (0.24 - 1.01)

5.2. Reactive Transport Model Simulations

5.2.1. Simulated base case conditions and results from scenario S1

Liquid saturation profiles and concentration of key aqueous species predicted at different times for the homogeneous sandy loam column are shown in Figure 5. The sandy loam vadose zone is computed to be 32% saturated with near atmospheric concentrations of O_2. As a result of oxic conditions, model results demonstrate significant residual NO_3^- concentration within the vadose zone (as would be expected). Evolving from these conditions, Figure 5 shows that with flooding scenario S1, water reaches depths of 490 cm and saturation levels reach 40% in the sandy loam column. Deeper in the column, lower saturation and only small decreases in O_2 concentration are predicted (Figure 5d, e). Calculated concentration profiles show that O_2 introduced with the infiltrating water is persistent at shallow depths down to 100 cm, below which O_2 declines slightly as floodwater moves below this zone. Model results further indicate higher NO_3^- reduction in the shallow vadose zone including the root zone (up to 100cm) with 35% of NO_3^- being denitrified (Figure 5f). Overall, this scenario results in NO_3^- concentration persisting at depth. While other redox reactions, such as iron reduction and HS^- reduction of NO_3^- to N_2, may be important, conditions needed to induce these reactions were not realized in the sandy loam vadose zone due to the high pore gas velocities of the homogenous sandy loam allowing for large amounts of O_2 to penetrate the profile from the incoming oxygenated water.

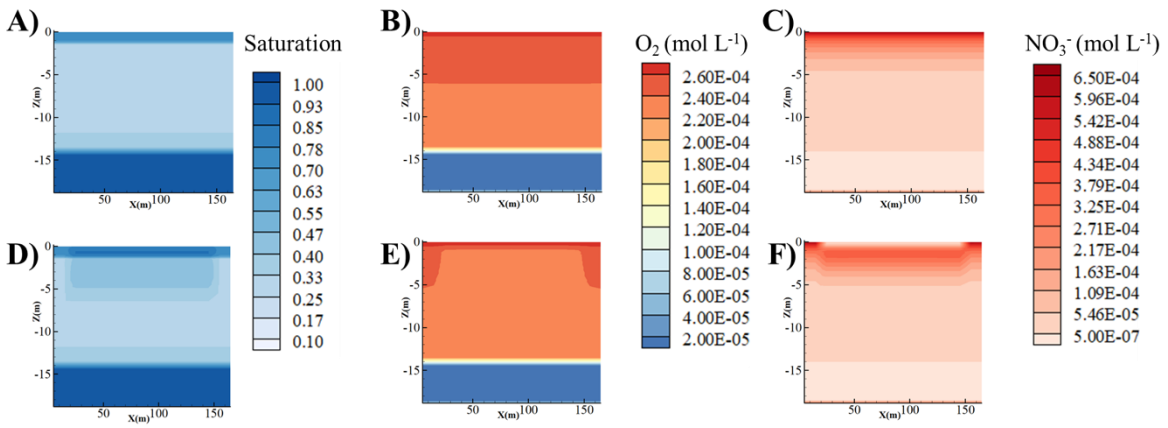

Figure 5: Homogeneous Sandy Loam: Predicted liquid saturation, O_2 (mol L^{-1}), and NO_3^- (mol L^{-1}) profiles at pre-flood steady state (A, B, and C, respectively) and 60 days from start of flooding for S1 (D, E, F).

In comparison to the homogenous sandy loam column, the predicted water content is higher (60% saturated) and O_2 concentration is 53% lower in the vadose zone of the homogenous silt loam column at steady state (Figure 6). This result is expected because of the difference in porosity, with silt loams having higher water holding capacity and lower pore gas velocities compared to sandy loams. Consequently, lower NO_3^- concentration and lower NO_3^-:Cl^- ratio are predicted in the silty loam vadose zone as compared to the sandy loam column (Figures 6 and 7). It is interesting to note that while greater NO_3^- loss and denitrification are predicted for the silty loam vadose zone, carbon concentration associated with the shallow vadose zone (below the root zone) are comparatively lower than for the sandy loam column. Moreover, the calculated pH is lower and iron concentrations are higher in the silt loam profile below the top meter when compared to the same depths within the sandy loam column (Figure 7). This suggests that chemolithoautotrophic reactions could be more important for these finer textured sediments. While both heterotrophic and chemolithoautotrophic reactions would be expected to result in a pH decrease (as expressed in Table 5), the greater decline in pH and concomitant increase in Fe^{+3} concentration suggests the importance of Fe and S redox cycling associated with the chemolithoautotrophic reactions in silty loam sediments (Figure 7).

Evolving from these steady state conditions, scenario S1 suggests that denitrification is enhanced as floodwater infiltrates into the silt loam column. Model results indicate that saturation increases to 80% from 1 to 4 m depths and O_2 decreases from 2.1 x 10^{-4} mol L^{-1} to 1.7 x 10^{-4} mol L^{-1}, resulting in 43% of the NO_3^- being denitrified for this scenario (**Figure** 8).

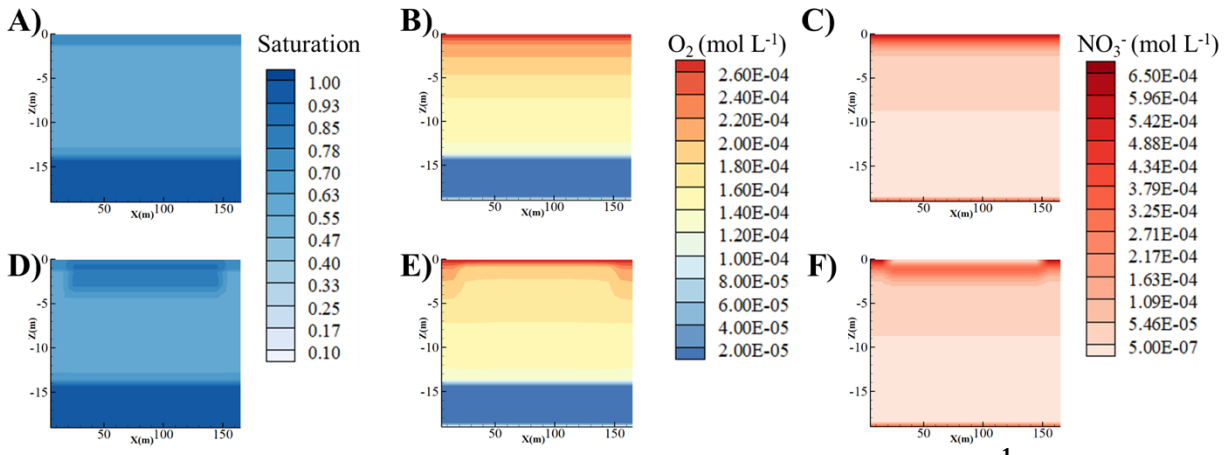

Figure 6: Homogeneous Silt Loam: Predicted liquid saturation, O_2 (mol L^{-1}), and NO_3^- (mol L^{-1}) profiles at pre-flood steady state (A, B, and C, respectively) and 60 days from start of flooding for S1 (D, E, F).

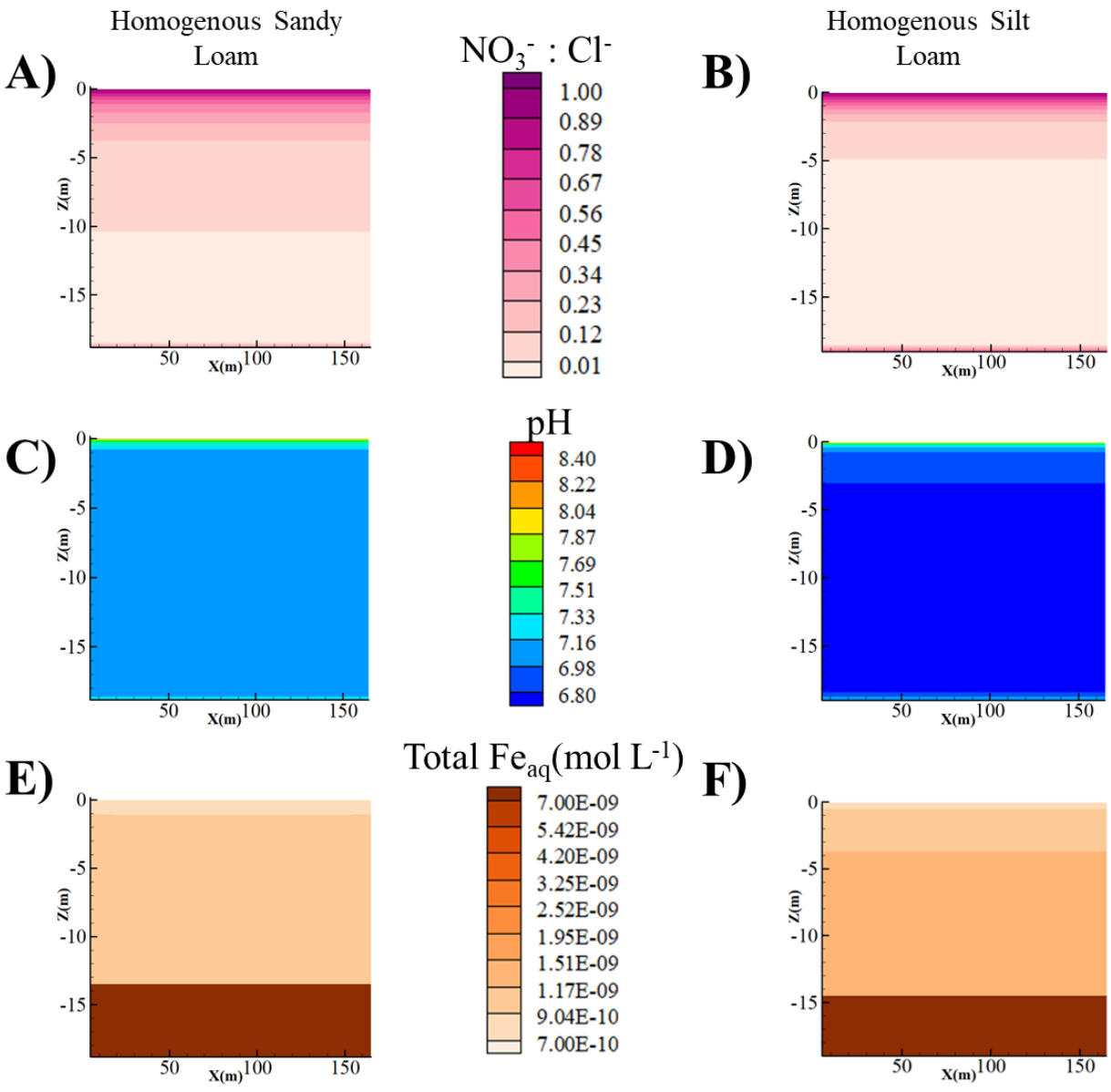

471

472

473 **Figure 7: Predicted NO_3^-:Cl (A and B), pH (C and D), and total $Iron_{aq}$ (E and F) (mol L^{-1}),**
474 **and total $Iron_{aq}$ (G and H) (mol L^{-1}) profiles for the homogeneous sandy loam vs.**
475 **homogeneous silt loam stratigraphies at pre-flood steady state.**

476

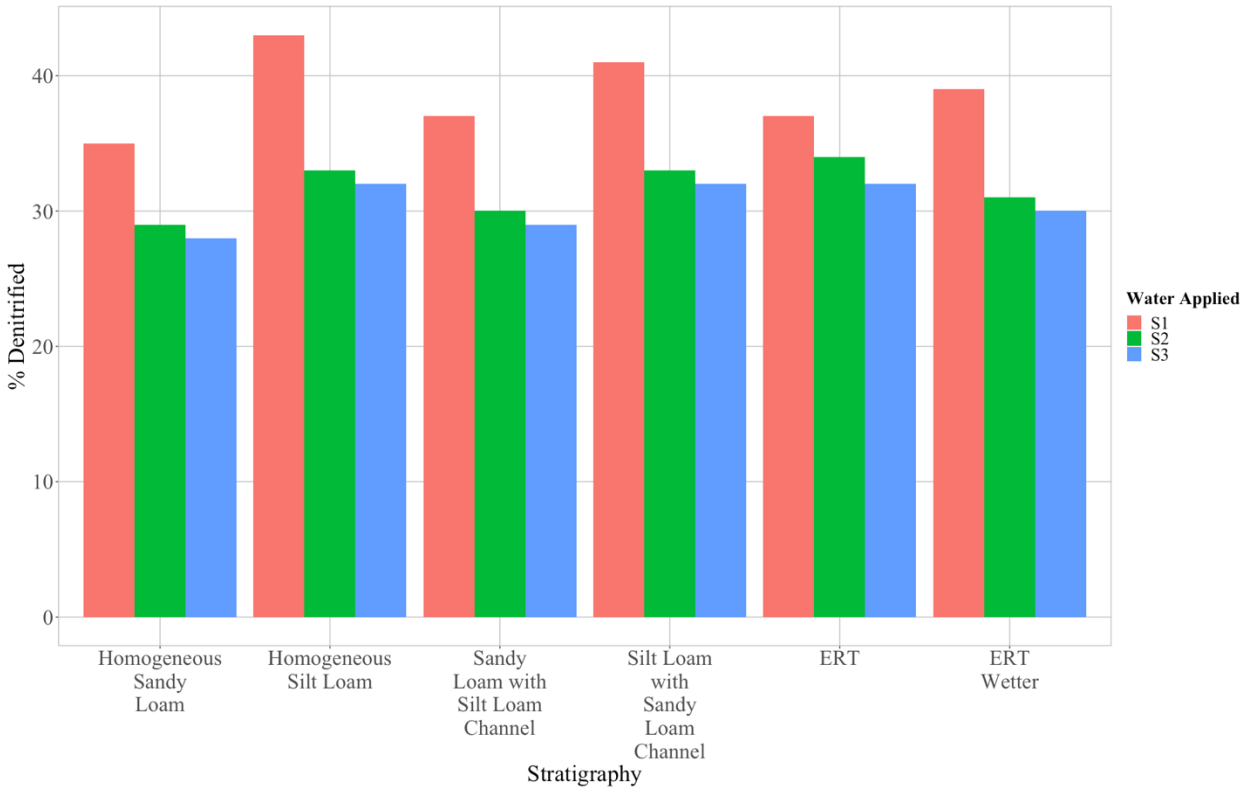

477

478 **Figure 8: Percent of NO_3^- denitrified for each stratigraphy and flooding scenario.**

479

480 In comparison to the homogeneous profiles, the sandy loam with silt loam channel
481 stratigraphy (SaSi case) has higher calculated water contents (60% saturated) and slightly lower
482 O_2 concentration within and surrounding the silt loam channel than the homogenous sandy loam
483 column under steady state conditions (Figure 9). Calculated NO_3^- concentrations are also similar
484 between the homogenous sandy loam column and SaSi case, except for within and below the silt
485 loam channel where lower NO_3^- concentration was predicted (Figure 9). For scenario S1, water
486 content for the SaSi case increased in a manner similar to the homogenous sandy loam, except
487 for within the silt loam channel, which increased from 60 to 81%. Figure 9 further demonstrates
488 that the infiltrating floodwater resulted in an increase in NO_3^- concentration between 1 and 3 m
489 within the sandy loam textured soil, but a decrease elsewhere. Within the channel itself, lower
490 nitrate and NO_3^-:Cl^- ratio are predicted, suggesting higher rates of denitrification (Figure 9).
491 Overall, the model results indicate that an average of 37% of the NO_3^- concentration is
492 denitrified in the SaSi case, with 35% denitrification occurring in the sandy loam matrix and
493 40% occurring within the silt loam channel. This suggests that the silt loam channel acts as a
494 denitrification hotspot. Furthermore, the silt loam channel has lower carbon and higher Fe^{+3}
495 concentrations similar to the homogenous silt loam column again suggesting the importance of
496 both heterotrophic and chemolithoautotrophic denitrification in these finer textured sediments.
497

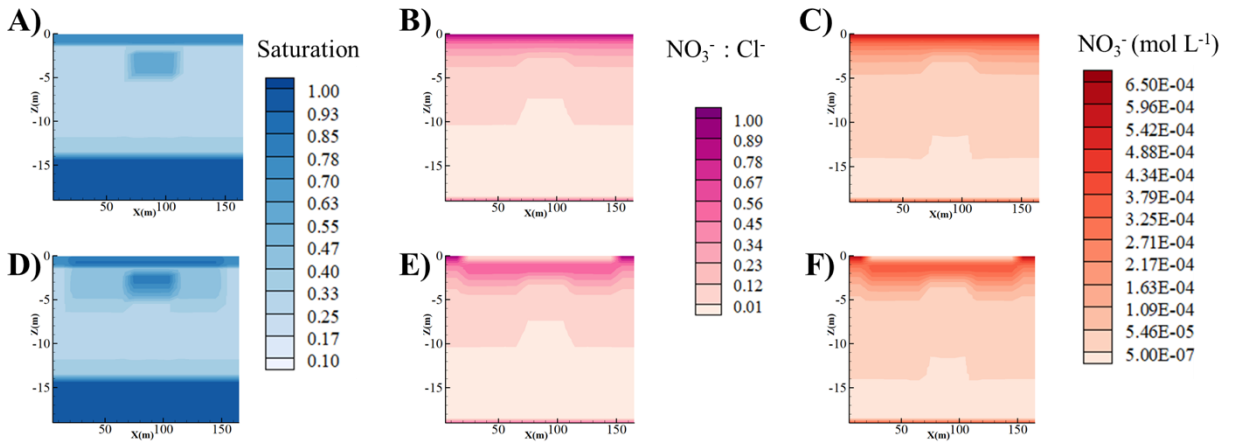

Figure 9: Sandy loam with silt loam channel (SaSi case) predicted liquid saturation, NO_3^-:Cl^- ratios, and NO_3^- (mol L^{-1}) profiles at pre-flood steady state (A, B, and C, respectively) and 60 days from start of flooding for S1 (D, E, F).

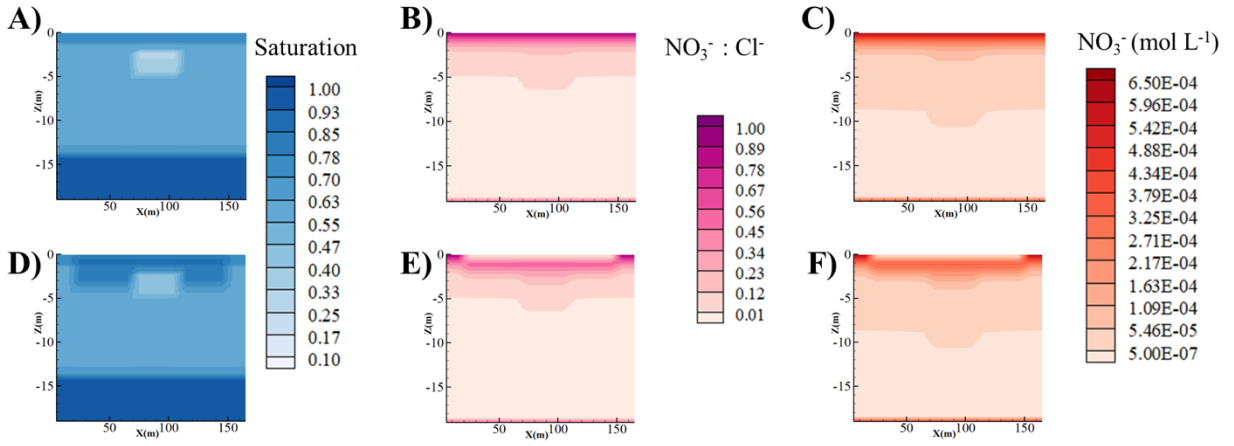

Figure 10: Silt loam with sandy loam channel (SiSa case) predicted liquid saturation, NO_3^-:Cl^- ratios, and NO_3^- (mol L^{-1}) profiles at pre-flood steady state(A, B, and C, respectively) and 60 days from start of flooding for S1 (D, E, F).

In comparison to the SaSi case, calculated water saturation and O_2 profiles were markedly different between the homogenous silt loam column and the silt loam with sandy loam channel (SiSa case) under steady state conditions (Figure 10). In particular, the sandy loam channel has lower calculated water content (32% saturation) than the homogenous silt loam column (60% saturation). Further, greater gas flux within the channel resulted in 11-19% higher O_2 concentration that penetrated deeper into the vadose zone as compared to the homogeneously textured column. NO_3^- concentration are also estimated to penetrate deeper into the vadose zone in the SiSa case due to the high permeability of the sandy loam channel (Figure 10). While carbon concentration also penetrated deeper in the vadose zone in the SiSa case, higher calculated O_2 concentration did not allow for comparable rates of denitrification in this case as observed in the homogenous silt loam profile. This is further confirmed by the lower NO_3^-:Cl^- ratio, which indicates that transport processes dominate biogeochemical fluxes within this

column (Figure 10). With scenario S1, the calculated water content increased to 48% saturation while the O_2 concentration remained the same within the channel. The high permeability channel allowed for NO_3^- to move faster and deeper into the vadose zone. Overall, calculated denitrification (41% of NO_3^- was denitrified) was lower in the SiSa case as compared to the homogeneous textured column.

In the simplified ERT stratigraphy, similar patterns were observed such that high permeability channels transported water, O_2, and NO_3^- faster and deeper into the subsurface than low permeability regions (Figure 11). As a result, concentration profiles showed significant variability across the modeled domain even under steady state conditions. For example, the calculated O_2 and NO_3^- concentrations are an order of magnitude lower in the shallow vadose zone below the claypan than within the preferential flow channel. Higher NO_3^-:Cl^- ratio within the channel further confirms that preferential flow paths transport higher quantities of dissolved aqueous species without their being impacted by other processes such as denitrification (Figure 11). Other interesting trends are shown by carbon and Fe^{+2} concentrations within the modeled column. Dissolved carbon in particular is predicted to have a lower concentration in the preferential flow channel and the matrix surrounding the channel than below the claypan layer. In contrast, the Fe^{+2} concentration is estimated to be higher in the matrix surrounding the preferential flow channel and below the claypan layer (not shown here). For scenario S1, model results indicate that NO_3^- moved through the preferential flow path faster and deeper into the profile, while the claypan acts as a denitrification barrier as evidenced by the decrease in NO_3^- :Cl^- ratio. The highest denitrification was estimated to occur in the matrix adjacent to the preferential flow channel (40% of NO_3^-), followed by intermediate nitrate reduction below the claypan and far away from the channel (38%), while the lowest denitrification was estimated to occur within the channel itself (34%). The confluence of higher amounts of C and NO_3^- moving into a reduced zone could be the reason that the matrix surrounding the preferential flow channel has higher denitrification rates, while the regions further away from the preferential flow channel have lower amounts of microbially available C and NO_3^-. In contrast, residence times are too short in the channel to allow for reducing conditions to develop. Overall, we find that low permeability zones alone (e.g., homogeneous silt loam) embedded within high flow zones (eg., matrix surrounding preferential flow channel, SiSa case) demonstrate highest denitrification rates across all soil profiles.

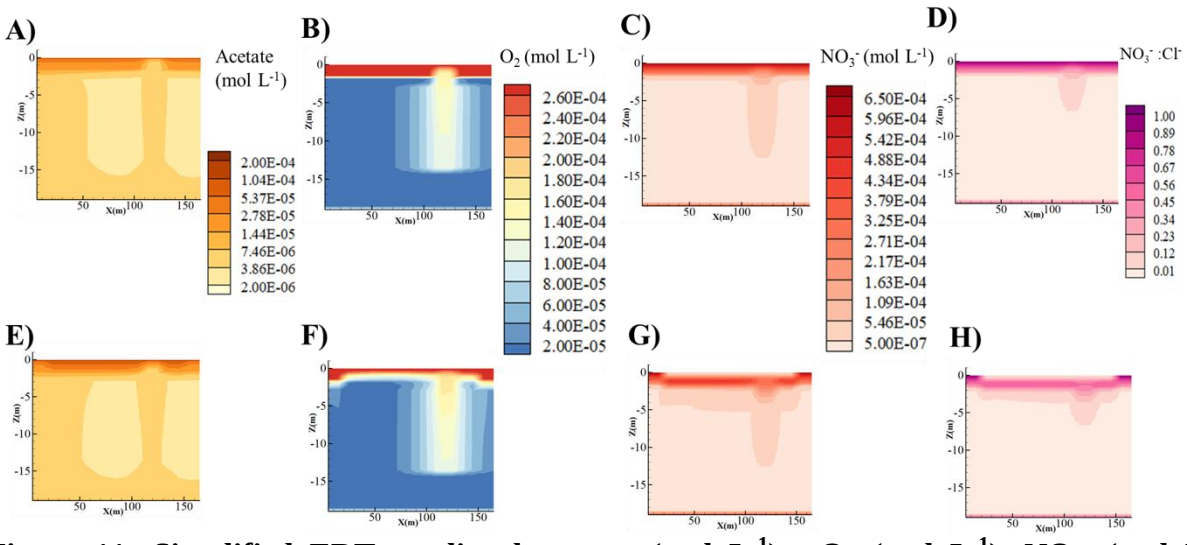

Figure 11: Simplified ERT predicted acetate (mol L^{-1}) , O_2 (mol L^{-1}), NO_3^- (mol L^{-1}) profiles, NO_3^-:Cl^- ratios at pre-flood steady state (A, B, C, and D respectively) and 60 days from start of flooding for S1 (E, F, G and H).

5.2.2. Results from scenarios S2 and S3

Because the ERT column is a realistic representation of our agricultural field site, we use this column to demonstrate the impact of hydraulic loading and application frequency on nitrogen fate and dynamics. Simulated profiles of liquid saturation, NO_3^-, NO_3^-:Cl^- and acetate for the simplified ERT stratigraphy for scenarios S2 (17 cm per week for four weeks) and S3 (17 cm two times per week for two weeks) are shown in Figure 12. It is interesting to note that AgMAR ponding under scenarios S2 and S3 resulted in fully saturated conditions to persist within the root zone (~ 100 cm depths) only. In comparison, the 68 cm all-at-once application for scenario S1 resulted in fully saturated conditions to occur at even greater depths of 235 cm (not shown here). This resulted in the NO_3^- front moving deeper into the subsurface to depths of 450 cm under S1 compared to 150 cm for scenarios S2 and S3 (Figure 12). Much lower concentrations of NO_3^- were found at 450 cm in scenarios S2 and S3 (8×10^{-6} mol NO_3^- L for both S2 and S3) compared to S1 (1×10^{-5} mol NO_3^- L). Thus, larger amounts of water applied all-at-once led to NO_3^- being transported faster and deeper into the profile.

Surprisingly, model results indicate 37% of NO_3^- was denitrified with scenario S1, while 34% and 32% of NO_3^- was denitrified in scenarios S2 and S3, respectively. For scenarios S2 and S3, denitrification was estimated to occur only within the root zone. This was confirmed by NO_3^-:Cl^- ratio that did not show any reduction with depth for these scenarios. A reason for this could be that acetate was not estimated to occur below the root zone, preventing electron donors from reaching greater depths for denitrification to occur. In contrast, model results for S1 indicate that acetate was leached down to 235 cm below the claypan layer. Overall, model results indicate that NO_3^- did not move as fast or as deep in scenarios S2 or S3; however, the ability of the vadose zone to denitrify was reduced when the hydraulic loading was decreased. The main reason for this was that breaking the application into smaller hydraulic loadings (17 cm) resulted in O_2 concentrations to recover to background atmospheric conditions faster than the larger (68 cm)

all-at-once application in scenario S1. In fact, the O_2 concentration differed slightly between S2 and S3. Because O_2 inhibits denitrification, we conclude that these conditions resulted in the different denitrification capacity across application frequency and duration. In summary, we find that larger amounts of water applied all-at-once increased the denitrification capacity of the vadose zone while incremental application of water did not. However, NO_3^- movement to deeper depths was slower under S2 and S3.

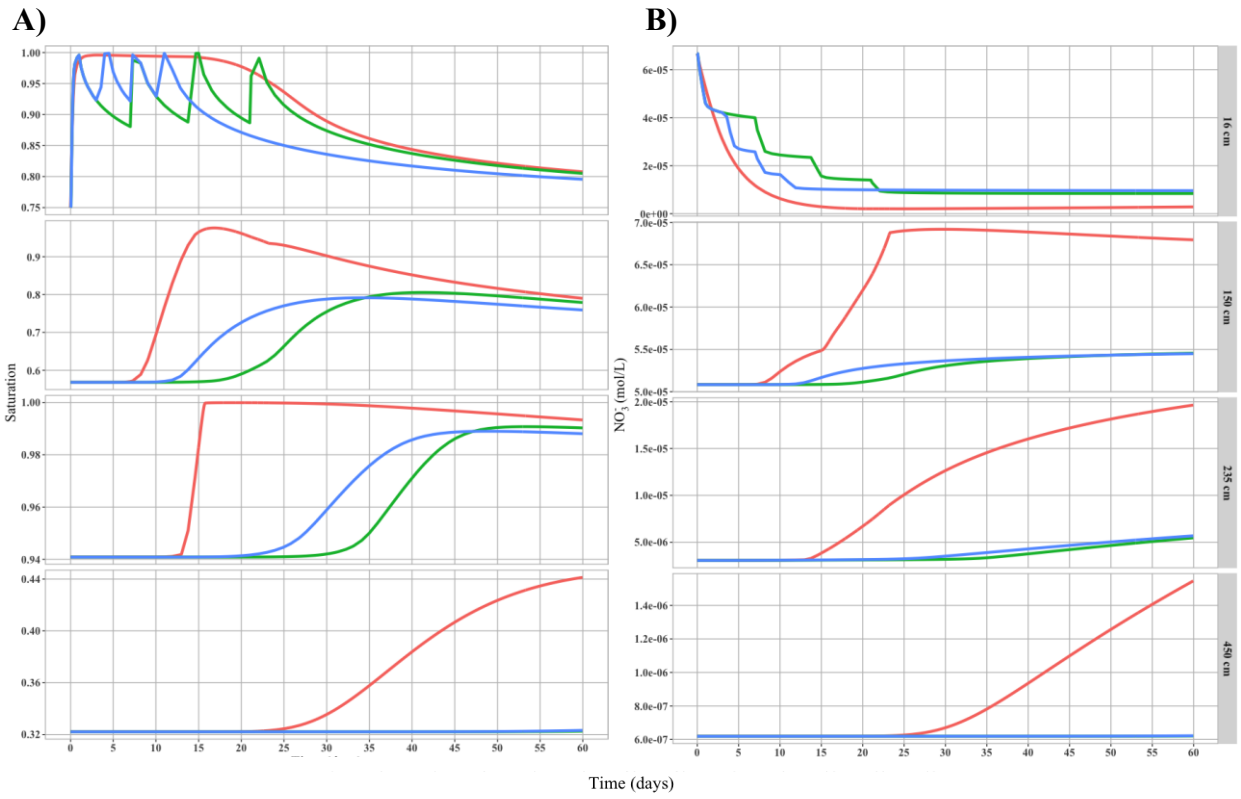

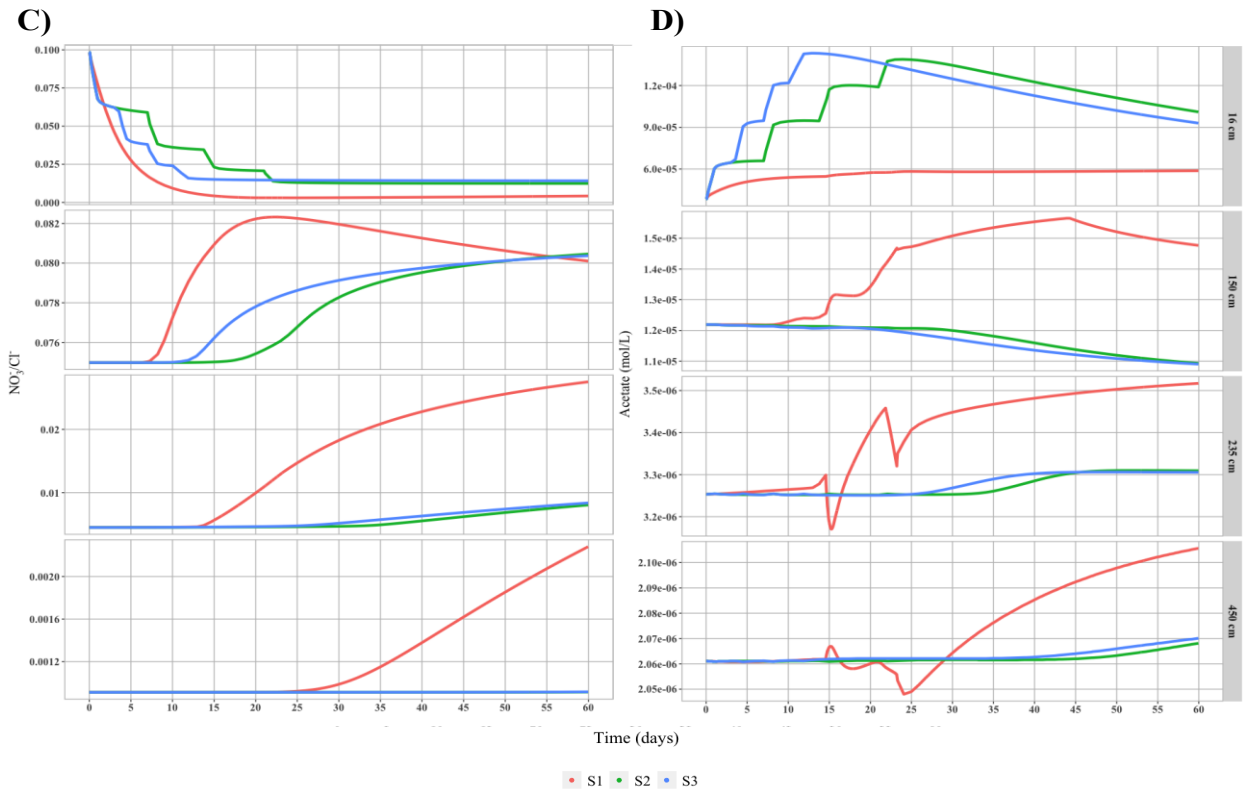

Figure 12: A) Saturation, B) NO_3^- (mol L^{-1}), C) ratio of NO_3^- to Cl^- and D) Acetate concentrations (mol L^{-1}), and over time by depth within each AgMAR scenario(S1, S2, S3) adjacent to the preferential flow channel for the Simplified ERT profile.

5.2.3. Results from varying Antecedent Moisture conditions

Because initial saturation conditions impact nitrogen leaching, we also simulated the impact of wetter antecedent moisture with 15% higher saturation levels than the base case simulation for the ERT profile. Simulated profiles of liquid saturation, NO_3^-, NO_3^-:Cl^- and acetate for the simplified ERT stratigraphy under wetter conditions are shown in Figure 13. Model results demonstrate that the water front moved faster and deeper into the soil profile under initially wetter conditions for all three scenarios. Within the shallow vadose zone (~150 cm), across AgMAR scenarios, O_2 concentrations were similar initially, but began differing at early simulated times, with lower O_2 under wetter antecedent moisture conditions than with the base-case simulation. In addition, both oxygen and nitrate concentrations showed significant spatial variation across the modeled column. Notably, nitrate concentrations were 166% (order of magnitude) higher in the preferential flow channel compared to the sandy loam matrix under wetter conditions, while only 161% difference was observed under the base case simulation (Figure 13).

Nitrate movement followed a pattern similar to water flow, with NO_3^- reaching greater depths with the wetter antecedent moisture conditions. Under S1, however, at 150 cm, NO_3^- decreased more quickly under the wetter antecedent moisture conditions due to biochemical reduction of NO_3^-, as evidenced by the decrease in NO_3^-:Cl^- ratio, as well as by dilution of the incoming floodwater. In the wetter antecedent moisture conditions, 39%, 31%, and 30% of NO_3^-

was denitrified under S1, S2, and S3, respectively. For S1, where water was applied all at once, more denitrification occurred in the wetter antecedent moisture conditions, however, the same was not true of S2 and S3 where water applications were broken up over time. This could be due to the hysteresis effect of subsequent applications of water occurring at higher initial moisture contents, allowing the NO_3^- to move faster and deeper into the profile without the longer residence times needed for denitrification to occur. Thus, wetter antecedent moisture conditions prime the system for increased denitrification capacity when water is applied all at once and sufficient reducing conditions are reached, however, this is counteracted by faster movement of NO_3^- into the vadose zone.

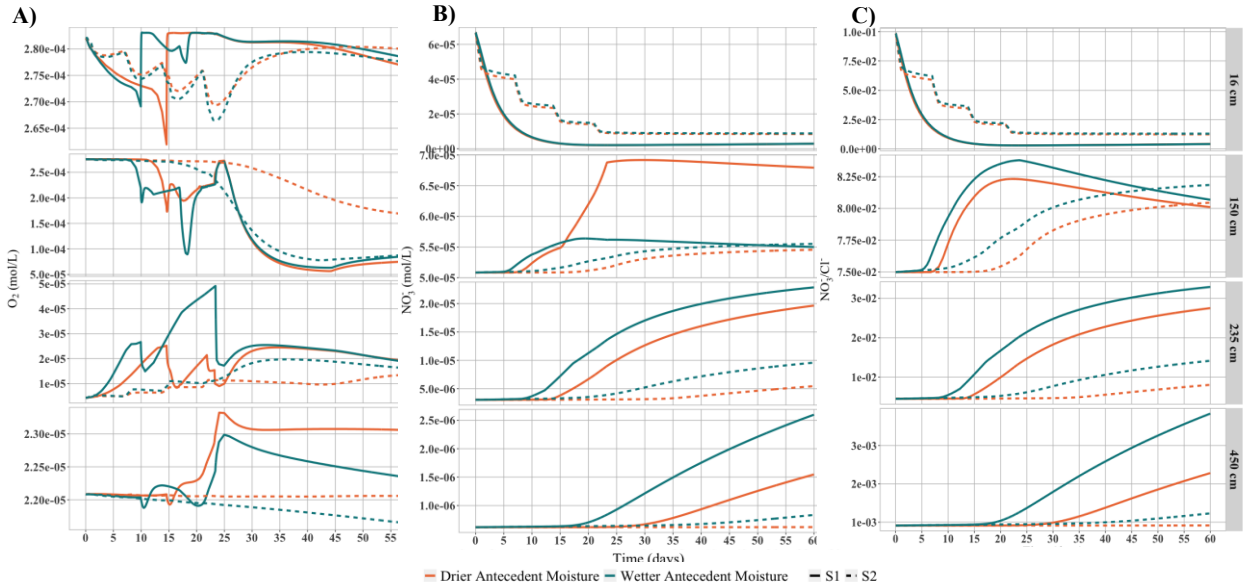

Figure 13: A) $O_{2\,(aq)}$ concentrations (mol L^{-1}), B) NO_3^- (mol L^{-1}), and C) ratio of NO_3^- to Cl^- over time by depth within AgMAR scenarios (S1 and S2) for different antecedent moisture conditions adjacent to the preferential flow channel.

6. Discussion

6.1. Impact of Stratigraphy

Because several characteristics of the vadose zone add complexity to modeling and understanding N cycling in agricultural soils, we used a reactive transport modeling framework to isolate and elucidate the effect of varying stratigraphic configurations and sediment types on N transformation and denitrification. Our results primarily demonstrate that low-permeability zones such as silt loams allow for reducing conditions to develop, thereby leading to higher denitrification in these sediments as compared to high permeability zones such as sandy loams. In fact, the homogenous silt loam profile reported the maximum amount of denitrification occurring across all five stratigraphic configurations (Figure 8). Furthermore, the presence of a silt loam channel in a dominant sandy loam column increased the capacity of the column to

637 denitrify by 2%. Conversely, adding a sandy loam channel into a silt loam matrix decreased the
638 capacity of the column to denitrify by 2%. These relatively simple heterogeneities exemplify
639 how hot spots in the deep vadose zone can have a small but accumulating effect on
640 denitrification capacity.
641 Another observation of interest for silty loams is the prominence of
642 chemolithoautotrophic reactions and Fe cycling observed in these sediments. In comparison,
643 sandy loam sediments showed persistence and transport of NO_3^- to greater depths. A reason for
644 this is that oxygen concentration was much more dynamic in sandy loams, rebounding to oxic
645 conditions more readily than in silt loams, even deep into the vadose zone (5 meters). Dutta et al.
646 (2015) found similar re-aeration patterns in a 1 m column experiment in a sand dominated soil,
647 with re-aeration occurring quickly once drying commenced. Even with the presence of a claypan,
648 defined by lower pore gas velocities and higher carbon concentration, a sandy loam channel
649 acted as a conduit of O_2 into the deep vadose zone maintaining a relatively oxic state and thus
650 decreasing the ability of the vadose zone to denitrify. Overall, denitrification capacity across
651 different lithologies was shown to depend on the tight coupling between transport, biotic
652 reactions as well as the cycling of Fe and S through chemolithoautotrophic pathways.
653

654 **6.2. Impact of Hydraulic Loading and Frequency**
655 Our results demonstrate that both hydraulic loading and frequency influenced the depth to
656 which NO_3^- reached, as well as the denitrification capacity of the subsurface. Given legacy
657 nitrate contamination is prevalent within the root zone of agricultural soils, we quantified the
658 amount of NO_3^- being lost from this zone across different loadings and duration of floodwater
659 application. Note that the root zone was made of the same soil texture across different
660 stratigraphic configurations, and accounted for a large proportion of denitrification in the system.
661 Under large hydraulic loadings (i.e., S1), lower denitrification was estimated in the root zone as
662 compared to the lower hydraulic loading scenarios (i.e., S2 or S3). However, overall
663 denitrification was estimated to be greatest under S1 when 68 cm of water was applied all-at-
664 once. The main reason for the higher denitrification capacity was the significant decline in O_2
665 concentration estimated for this scenario, whereas such conditions could not be maintained
666 below one meter with lower hydraulic loadings under scenarios S2 and S3. It seems that there
667 may exist a threshold hydraulic loading and frequency of application that could result in anoxic
668 conditions and therefore promote denitrification within the vadose zone for different
669 stratigraphic configurations, although this was not further explored in this study. In another
670 study, Schmidt et al. (2011) found a threshold infiltration rate of 0.7 m d^{-1} for a three-hectare
671 recharge pond located in the Pajaro Valley of central coastal California, such that no
672 denitrification occurred when this threshold was reached.
673 Our results further indicate that higher hydraulic loading, in addition to causing increased
674 levels of saturation and decrease in O_2, resulted in leaching of DOC to greater depths in
675 comparison to lower hydraulic loading scenarios (i.e., S2, S3). Akhavan et al. 2013 found similar
676 results for an infiltration basin wherein 1.4% higher DOC levels were reported at depths down to
677 4 m when hydraulic loading was increased. Because organic carbon is typically limited to top 1
678 m in soils (Dwivedi et al., 2018), leached DOC that has not been microbially processed could be
679 an important source of electron donors for denitrification at depth. This finding can be exploited

in agricultural soils by using cover crop and other management practices that increase soluble carbon at depth and therefore remove residual N from the vadose zone.

While lower denitrification capacity was estimated for scenarios S2 and S3, an advantage of incremental application was that NO_3^- concentration was not transported to greater depths. Thus, higher NO_3^- concentration was confined to the root zone. If NO_3^- under these scenarios stays closer to the surface, where microbial biomass is higher, and where roots, especially in deep rooted perennial systems such as almonds, can access it, it could ultimately lead to less NO_3^- lost to groundwater. While there is potential for redistribution of this NO_3^- via wetting and drying cycles, future modeling studies should explore multi-year AgMAR management strategies combined with root dynamics to understand N cycling under long-term AgMAR.

6.3. Impact of Antecedent Moisture

Simulation results indicate that wetter antecedent moisture conditions promote water and NO_3^- to move deeper into the domain compared to the drier base case simulation. This finding has been noted previously in the literature, however, disagreement exists on the magnitude and extent to which antecedent moisture conditions affect water and solute movement and is highly dependent on vadose zone characteristics. For example, in systems dominated by macropore flow, higher antecedent soil moisture increased the depth to which water and solutes were transported (McCoy et al. 1994, Jarvis et al. 2007). In a soil with textural contrast, where hydraulic conductivity between the topsoil and subsoil decreases sharply, drier antecedent moisture conditions caused water to move faster and deeper into the profile compared to wetter antecedent moisture conditions (Hardie et al. 2011). In our system, where a low-permeability layer (i.e., claypan) lies above a high permeability layer (i.e., sandy loam), the reverse trend was observed. Thus, a tight coupling of stratigraphic heterogeneity and antecedent moisture conditions interact to affect both NO_3^- transport and cycling in the vadose zone, which should be considered while designing AgMAR management strategies to reduce NO_3^- contamination of groundwater.

7. Conclusion

Agricultural managed aquifer recharge is a promising management strategy to increase groundwater recharge. However, to ensure adoption of the practice, AgMAR must not compromise groundwater quality. To quantify the influence of AgMAR on groundwater quality, specifically nitrate, we tested different AgMAR application rates under different stratigraphic configurations and antecedent moisture conditions using a reactive transport modeling framework. Our results indicate that fine textured sediments by themselves (e.g., homogeneous silt loam) or embedded within high permeability zones (e.g., silt loam channel within sandy loam sediments, matrix surrounding preferential flow channels) demonstrate highest denitrification capacity across different stratigraphic configurations. Further, in comparing AgMAR strategies, we found that denitrification capacity increased by applying large amounts of water all-at-once rather than in small incremental amounts. However, applying water all-at-once also pushes NO_3^- deeper into the soil profile compared to applying water in increments, especially if wetter antecedent moisture conditions exist. We conclude that ideal incremental AgMAR applications and hydraulic loadings can be designed to promote denitrification within the root zone and prevent N leaching to groundwater, but this treatment depends on the underlying stratigraphy and site characteristics. Therefore, the site's underlying geology, initial soil moisture content, and

depth to the water table influences the water quality outcomes of implementing AgMAR. We recommend future studies to focus on the multiyear effects of AgMAR on N cycling, as well as management practices (i.e. cover cropping) that reduce residual N and increase labile DOC movement into the deep subsurface to increase available electron donors for denitrification.

Acknowledgements

This material is based upon work supported as part of the DOE-SCGSR project, which is funded by the U.S. Department of Energy Biological and Environmental Science Priority Research Area, and as part of the Watershed Function Science Focus Area, which is funded by the U.S. Department of Energy, Office of Science, Office of Biological and Environmental Research, under Award Number DE-AC02-05CH11231 to Lawrence Berkeley National Laboratory. Partial support provided by Lawrence Berkeley Laboratory's Directed Research and Development Program. Additionally, this work was supported by a grant from the Almond Board of California. Data for determining how the data clustered can be found in Waterhouse et al. (in prep) and on the ESS-DIVE repository hosted by Lawrence Berkeley National Lab. The data gathered for this project would not be possible without the help of technicians, graduate and undergraduate students: Feifan Yang, Zaira Joaquin-Morales, and Rebecca Serata.

References

1. Akhavan, M., Imhoff, P.T., Andres, A.S., Finsterle, S., 2013. Model evaluation of denitrification under rapid infiltration basin systems. J. Contam. Hydrol. 152, 18–34. https://doi.org/10.1016/j.jconhyd.2013.05.007
2. Arora, B., Mohanty, B.P., McGuire, J.T., Cozzarelli, I.M. 2013. Temporal dynamics of biogeochemical processes at the Norman Landfill site. *Water Resources Research*, *49*(10), pp.6909-6926.
3. Arora B., Sengör S.S., Steefel C.I. 2015. A reactive transport benchmark on heavy metal cycling in lake sediments. Comput. Geosci. 19:613–633. doi:10.1007/s10596-014- 9445-8
4. Arora, B., Spycher, N.F., Steefel, C.I., Molins, S., Bill, M., Conrad, M.E., Dong, W., Faybishenko, B., Tokunaga, T.K., Wan, J., Williams, K.H., Yabusaki, S.B., 2016. Influence of hydrological, biogeochemical and temperature transients on subsurface carbon fluxes in a flood plain environment. Biogeochemistry 127, 367–396. https://doi.org/10.1007/s10533-016-0186-8
5. Ascott, M.J., Gooddy, D.C., Wang, L., Stuart, M.E., Lewis, M.A., Ward, R.S., Binley, A.M., 2017. Global patterns of nitrate storage in the vadose zone. Nat. Commun. 8, 1416. https://doi.org/10.1038/s41467-017-01321-w
6. Ascott, M.J., Wang, L., Stuart, M.E., Ward, R.S., Hart, A., 2016. Quantification of nitrate storage in the vadose (unsaturated) zone: a missing component of terrestrial N budgets. Hydrol. Process. 30, 1903–1915. https://doi.org/10.1002/hyp.10748
7. Bachand, P.A.M., Roy, S.B., Choperena, J., Cameron, D., Horwath, W.R., 2014. Implications of using on-farm flood flow capture to recharge groundwater and mitigate flood risks along the Kings River, CA. Environ. Sci. Technol. 48, 13601–13609. https://doi.org/10.1021/es501115c
8. Baram, S., Couvreur, V., Harter, T., Read, M., Brown, P.H., Kandelous, M., Smart, D.R., Hopmans, J.W., 2016. Estimating Nitrate Leaching to Groundwater from Orchards: Comparing Crop Nitrogen Excess, Deep Vadose Zone Data-Driven Estimates, and HYDRUS Modeling. Vadose Zo. J. 15, 0. https://doi.org/10.2136/vzj2016.07.0061
9. Bonin, P., Gilewicz, M., Bertrand, J.C., 1989. Effects of oxygen on each step of denitrification on Pseudomonas nautica. Can. J. Microbiol. 35, 1061–1064. https://doi.org/10.1139/m89-177
10. Brockman FJ, Kieft TL, Fredrickson JK, Bjornstad BN, Li SW, Spangenburg W, Long PE 1992. Microbiology of vadose zone paleosols in south-central Washington State. Microb Ecol 23:279-301.
11. Botros, Farag E, Onsoy, Yuksel S, Ginn, Timothy R, Harter, T., 2012. Richards Equation - Based Modeling to Estimate Flow and Nitrate Transport in a Deep Alluvial Vadose Zone. Vadoes Zo. J. 11. https://doi.org/10.2136/vzj2011.0145
12. Bundt, M., Widmer, F., Pesaro, M., Zeyer, J., Blaser, P., 2001. Preferential flow paths: Biological "hot spots" in soils. Soil Biol. Biochem. 33, 729–738. https://doi.org/10.1016/S0038-0717(00)00218-2
13. Butterbach-Bahl, K., Baggs, E.M., Dannenmann, M., Kiese, R., Zechmeister-Boltenstern, S., 2013. Nitrous oxide emissions from soils: how well do we understand the processes and their controls? Philos. Trans. R. Soc. Lond. B. Biol. Sci. 368, 20130122. https://doi.org/10.1098/rstb.2013.0122
14. California Department of Food and Agriculture. Crop Report 2017. http://www.stanag.org/pdf/cropreport/cropreport2017.pdf
15. Carlson, H.K., Clark, lain C., Melnyk, R.A., Coates, J.D., 2012. Toward a mechanistic understanding of anaerobic nitrate-dependent iron oxidation: Balancing electron uptake and detoxification. Front. Microbiol. 3, 1–6. https://doi.org/10.3389/fmicb.2012.00057
16. Chaopricha, N.T., Marín-spiotta, E., 2013. Soil burial contributes to deep soil organic carbon storage. Soil Biol. Biochem. 69, 251–264.
17. Cressey, E.L., Dungait, J.A.J., Jones, D.L., Nicholas, A.P., Quine, T.A., 2018. Soil microbial populations in deep floodplain soils are adapted to infrequent but regular carbon substrate addition. Soil Biol. Biochem. 122, 60–70. https://doi.org/10.1016/j.soilbio.2018.04.001
18. Doane, T.A., Horwath, W.R., 2003. Spectrophotometric Determination of Nitrate with a Single Reagent. Analytical Letters 36, 2713–2722.
19. Doussan et al. 1997 River bank filtration: modelling of the changes in water chemistry with emphasis on nitrogen species. Journal of Contaminant Hydrology 25 (1997) 129-156.
20. Dutta, T., Carles-Brangarí, A., Fernàndez-Garcia, D., Rubol, S., Tirado-Conde, J., Sanchez-Vila, X., 2015. Vadose zone oxygen (O2) dynamics during drying and wetting cycles: An artificial recharge laboratory experiment. J. Hydrol. 527, 151–159. https://doi.org/10.1016/j.jhydrol.2015.04.048

21. Dwivedi, D., Arora, B., Steefel, C.I., Dafflon, B., Versteeg, R. 2018. Hot spots and hot moments of nitrogen in a riparian corridor. *Water Resources Research*, *54*(1), pp.205-222.
22. Groffman, P.M., Holland, E.A., Myrold, D.D., Robertson, G.P., Zou, X. 1999. Denitrification. Pages 272-288 in G.P. Robertson, D.C. Coleman, C.S. Bledsoe, P. Sollins (editors). Standard soil methods for long-term ecological research. Oxford University Press, New York, NY, USA.
23. Handley KM, VerBerkmoes NC, Steefel CI et al (2013) Bios- timulation induces syntrophic interactions that impact C, S and N cycling in a sediment microbial community. ISME J 7:800–816. doi:10.1038/ismej.2012.148
24. Hanson, B.R., Šimůnek, J., Hopmans, J.W., 2006. Evaluation of urea-ammonium-nitrate fertigation with drip irrigation using numerical modeling. Agric. Water Manag. 86 (1), 102–113.
25. Harden G.W., 1987. Soils Developed in Granitic Alluvium near Merced, California. U.S. GEOLOGICAL SURVEY BULLETIN 1590-A
26. Harter, T., Onsoy, Y.S., Heeren, K., Denton, M., Weissmann, G., Hopmans, J.W., Horwath, W.R., 2008. Deep vadose zone hydrology demonstrates fate of nitrate in eastern San Joaquin Valley. Calif. Agric. 59, 124–132. https://doi.org/10.3733/ca.v059n02p124
27. Hunter K.S., Wang Y., Van Cappellen P. 1998. Kinetic modeling of microbially-driven redox chemistry of subsurface environments: coupling transport, microbial metabolism and geochemistry. J. Hydrol. 209:53–80. doi:10.1016/ S0022-1694(98)00157-7
28. Jardine, P.M., Mayes, M. a., Mulholland, P.J., Hanson, P.J., Tarver, J.R., Luxmoore, R.J., McCarthy, J.F., Wilson, G. V., 2006. Vadose Zone Flow and Transport of Dissolved Organic Carbon at Multiple Scales in Humid Regimes. Vadose Zo. J. 5, 140. https://doi.org/10.2136/vzj2005.0036
29. Jahangir, M.M.R., Khalil, M.I., Johnston, P., Cardenas, L.M., Hatch, D.J., Butler, M., Barrett, M., O'flaherty, V., Richards, K.G., 2012. Denitrification potential in subsoils: A mechanism to reduce nitrate leaching to groundwater. Agric. Ecosyst. Environ. 147, 13–23. https://doi.org/10.1016/j.agee.2011.04.015
30. Kirschbaum, M.U.F., 1995. The temperature dependence of soil organic matter decomposition, and the effect of global warming on soil organic C storage. Soil Biol. Biochem. 27, 753–760. https://doi.org/10.1016/0038-0717(94)00242-S
31. Kocis, T.N., Dahlke, H.E., 2017. Availability of high-magnitude streamflow for groundwater banking in the Central Valley, California. Environ. Res. Lett. 12. https://doi.org/10.1088/1748-9326/aa7b1b
32. Landon M.K., Belitz K. 2006, Ground-Water Quality Data in the Central Eastside San Joaquin Basin 2006: Results from the California GAMA Program. USGS Data Series 325, In cooperation with the California State Water Resources Control Board
33. Lovley, D.R., Phillips, E.J.P., 1987. Rapid assay for microbially reducible ferric iron in aquatic sediments. Appl. Environ. Microbiol. 53, 1536–1540. https://doi.org/10.1007/BF01611203
34. Maggi et al. 2008 A mechanistic treatment of the dominant soil nitrogen cycling processes: Model development, testing, and application. JOURNAL OF GEOPHYSICAL RESEARCH, VOL. 113, G02016, doi:10.1029/2007JG000578, 2008
35. Marín-Spiotta, E., Chaopricha, N.T., Plante, A.F., Diefendorf, A.F., Mueller, C.W., Grandy, A.S., Mason, J.A., 2014. Long-term stabilization of deep soil carbon by fire and burial during early Holocene climate change. Nat. Geosci. 7, 428–432. http://dx.doi.org/10. 1038/ngeo2169.
36. Mayer KU, Frind EO, Blowes DW (2002) Multicomponent reactive transport modeling in variably saturated porous media using a generalized formulation for kinetically controlled reactions. Water Resour Res 38:13–1–13–21. doi: 10.1029/2001WR000862
37. McCoy, E.L., Boast, C.W., Stehouwer, R.C., Kladivko, E.J., 1994. Macropore hydraulics: taking a sledgehammer to classical theory. In: Lal, R., Stewart, B.A. (Eds.), Soil Processes and Water Quality. Lewis Publishers, Boca Raton. p. 303-348.
38. Meyer, N., Meyer, H., Welp, G., Amelung, W., 2018. Soil respiration and its temperature sensitivity (Q10): Rapid acquisition using mid-infrared spectroscopy. Geoderma 323, 31–40. https://doi.org/10.1016/j.geoderma.2018.02.031
39. Morel FMM, Hering JG (1993) Principles and applications of aquatic chemistry. Wiley, New York
40. Neal, R.H., G . Sposito, K.M. Holtzclaw, and S.J. Traina. 1987. Selenite adsorption on alluvial soils: I. Soil composition and pH effects. Soil Sci. Soc. Am. J. 51:1161-1165
41. Palmer K, Drake HL, Horn MA (2010) Association of novel and highly diverse acid-tolerant denitrifiers with N2O fluxes of an acidic fen. Appl Environ Microbiol 76:1125–1134. doi:10.1128/AEM.02256-09

42. Phogat, V., Skewes, M.A., Cox, J.W., Sanderson, G., Alam, J., Simunek, J. "Seasonal simulation of water, salinity and nitrate dynamics under drip irrigated mandarin (Citrus reticulata) and assessing management options for drainage and nitrate leaching." *Journal of Hydrology* 513 (2014): 504-516.
43. Pratt, P.F., Jones, W., Hunsaker, V.E., 1972. Nitrate in Deep Soil Profiles in Relation to Fertilizer Rates and Leaching Volume. J. Environ. Qual. 1, 97–102.
44. Pruess, K., Oldenburg, C., Moridis, G., 1999. TOUGH2 User's Guide, Version 2.0. Lawrence Berkeley National Laboratory Report LBNL-43134.
45. Rodell, M., Famiglietti, J.S., Wiese, D.N., Reager, J.T., Beaudoing, H.K., Landerer, F.W., Lo, M.-H., 2018. Emerging trends in global freshwater availability. Nature 1. https://doi.org/10.1038/s41586-018-0123-1
46. Salehi, A., Navabian, M., Varaki, M.E., Pirmoradian, N., 2017. Evaluation of HYDRUS-2D model to simulate the loss of nitrate in subsurface controlled drainage in a physical model scale of paddy fields. Paddy Water Environ. 15, 433–442. https://doi.org/10.1007/s10333-016-0561-z
47. Schaap, M.G., Leij, F.J., van Genuchten, M.T. 2001. Rosetta: a computer program for estimating soil hydraulic parameters with hierarchical pedotransfer functions. J. Hydrol. 251, 163-176
48. Schmidt, C.M., Fisher, A.T., Racz, A.J., Lockwood, B.S., Huertos, M.L., 2011. Linking denitrification and infiltration rates during managed groundwater recharge. Environ. Sci. Technol. 45, 9634–9640. https://doi.org/10.1021/es2023626
49. Soil Survey Laboratory Methods Manual. 2004. Texture by Pipette Analysis. Soil Survey Investigations Report No. 42. V. 4. p. 14-21.
50. Sonnenthal, Eric, Spycher, Nicolas, and USDOE. *TOUGHREACT (TREACT) v3.32*. Computer software. USDOE. 28 Feb. 2014. Web. doi:10.11578/dc.20190130.1.
51. Stookey, L.L., 1970. Ferrozine-A New Spectrophotometric Reagent for Iron. Anal. Chem. 42, 779–781. https://doi.org/10.1021/ac60289a016
52. Syswerda, S.P., Corbin, A.T., Mokma, D.L., Kravchenko, A.N., Robertson, G.P. 2011. Agricultural management and soil carbon storage in surface versus deep layers. Soil Sci. Soc. Amer. Journal. 75: 92-101.
53. Thomas, G., 1996. Soil pH and soil acidity. In: Sparks, D.L. (Ed.), Methods of soil analysis. Part 3. Chemical methods. Soil Sci. Soc. Am.pp. 475–490 (Madison WI). Throckmorton,
54. van der Laan, M., Annandale, J.G., Bristow, K.L., Stirzaker, R.J., Du Preez, C.C., Thorburn, P.J., 2013. Modelling nitrogen leaching: Are we getting the right answer for the right reason? Agric. Water Manag. 133, 74–80. https://doi.org/10.1016/j.agwat.2013.10.017
55. Van Meter, K.J., Basu, N.B., Veenstra, J.J. and Burras, C.L., 2016. The nitrogen legacy: emerging evidence of nitrogen accumulation in anthropogenic landscapes. Environmental Research Letters, 11(3), p.035014.
56. Waterhouse H, Bachand S, Mountjoy D, Choperena J, Bachand P, Dahlke H, Horwath W. 2020. Agricultural managed aquifer recharge — water quality factors to consider. Calif Agr 74(3):144-154. https://doi.org/10.3733/ca.2020a0020.
57. Weissmann, G.S., Mount, J.F., and Fogg, G.E., 2002a, Glacially driven cycles in accumulation space and sequence stratigraphy of a stream dominated alluvial fan, San Joaquin Valley, California, U.S.A.: Journal of Sedimentary Research, v. 72, no. 2, p. 240–251.
58. Weissmann, G.S., Zhang, Y., LaBolle, E.M., and Fogg, G.E., 2002b, Dispersion of groundwater age in an alluvial aquifer system: Water Resources Research, v. 38, p. 1198–1211, doi: 10.1029/2001WR000907.
59. White A.F., Blum A.E., Schulz M.S., Bullen T.D., Harden J.W., Peterson M.L., 1996. Chemical weathering rates of a soil chronosequence on granitic alluvium: I. Quantification of mineralogical and surface area changes and calculation of primary silicate reaction rates. Geochimica et Cosmochimica Acta, Vol. 60, No. 14, pp. 2533-2550
60. Wu Y, Ajo-Franklin JB, Spycher N et al (2011) Geophysical monitoring and reactive transport modeling of ureolyti- cally-driven calcium carbonate precipitation. Geochem Trans 12:7. doi:10.1186/1467-4866-12-7
61. Xu, T., Sonnenthal, E. L., Spycher, N., and Zheng, L. (2017), TOUGH- REACT—A simulation program for non-isothermal multiphase reactive geochemical transport in variably saturated geologic media: Applications to geothermal injectivity and CO2 geological sequestration, Comput. Geosci., 32(2), 145–165.
62. Yabusaki, S.B., Wilkins, M.J., Fang, Y., Williams, K.H., Arora, B., Bargar, J., Beller, H.R., Bouskill, N.J., Brodie, E.L., Christensen, J.N., Conrad, M.E., Danczak, R.E., King, E., Soltanian, M.R., Spycher, N.F, Steefel, C.I., Tokunaga, T.K., Versteeg, R., Waichler, S.R., Wainwright, H.M. *Environmental Science & Technology* **2017** *51* (6), 3307-3317 DOI: 10.1021/acs.est.6b04873

903
904